

# A Brain-to-Population Graph Learning Framework for Diagnosing Brain Disorders

Qianqian Liao<sup>a</sup>, Wuque Cai<sup>a</sup>, Hongze Sun<sup>a</sup>, Dongze Liu<sup>a</sup>, Duo Chen<sup>a,b</sup>, Dezhong Yao<sup>a,c,\*</sup>, Daqing Guo<sup>a,c,\*</sup>

<sup>a</sup>Clinical Hospital of Chengdu Brain Science Institute, MOE Key Lab for NeuroInformation, China-Cuba Belt and Road Joint Laboratory on Neurotechnology and Brain-Apparatus Communication, School of Life Science and Technology, University of Electronic Science and Technology of China, Chengdu 611731, China.

<sup>b</sup>School of Artificial Intelligence, Chongqing University of Education, Chongqing 400065, China.

<sup>c</sup>Research Unit of NeuroInformation (2019RU035), Chinese Academy of Medical Sciences, Chengdu 611731, China.

---

## Abstract

Recent developed graph-based methods for diagnosing brain disorders using functional connectivity highly rely on predefined brain atlases, but overlook the rich information embedded within atlases and the confounding effects of site and phenotype variability. To address these challenges, we propose a two-stage Brain-to-Population Graph Learning (B2P-GL) framework that integrates the semantic similarity of brain regions and condition-based population graph modeling. In the first stage, termed brain representation learning, we leverage brain atlas knowledge from GPT-4 to enrich the graph representation and refine the brain graph through an adaptive node reassignment graph attention network. In the second stage, termed population disorder diagnosis, phenotypic data is incorporated into population graph construction and feature fusion to mitigate confounding effects and enhance diagnosis performance. Experiments on the ABIDE I, ADHD-200, and Rest-meta-MDD datasets show that B2P-GL outperforms state-of-the-art methods in prediction accuracy while enhancing interpretability. Overall, our proposed framework offers a reliable and personalized approach to brain disorder diagnosis, advancing clinical applicability.

**Keywords:** Graph neural network, Brain disorder, Functional connectivity, Brain atlas.

---

## 1. Introduction

Brain disorders—including neurodevelopmental conditions such as Autism Spectrum Disorder (ASD)(Hodges et al., 2020) and Attention-Deficit/Hyperactivity Disorder (ADHD) (Hinshaw, 2018), as well as psychiatric disorders like Major Depressive Disorder (MDD)—significantly impair cognitive, emotional, and social functioning. These conditions not only limit individuals’ potential but also place substantial burdens on families, communities, and healthcare systems (Arora et al., 2018). Early and accurate identification and intervention are critical to mitigate these impacts and improve outcomes for affected individuals (Finlay-Jones et al., 2019).

Functional magnetic resonance imaging (fMRI) is a non-invasive technique for measuring brain activity through blood-oxygen-level-dependent (BOLD) signals (Logothetis, 2003), offering critical insights into complex neurological disorders (Park and Friston, 2013; Arbabshirani et al., 2017; Tang et al., 2023). As a widely used metric for quantifying synchronized BOLD activity, functional connectivity (FC) assesses interregional communication by analyzing temporal correlations between brain regions partitioned using predefined atlases (Roland and Zilles, 1994; Logothetis and Wandell, 2004). However, existing approaches to FC analysis fail to utilize the rich medical information in these atlases, such as functional characteristics and structural organization of brain regions, which could improve the interpretation of fMRI data

(Zhang et al., 2024). Moreover, a major challenge in utilizing fMRI databases for neuroscience research lies in the presence of confounding effects, arising from site-related differences (e.g., MRI machine vendors) and population heterogeneity (e.g., age, gender) (Gordon and Nelson, 2021; Geerlings et al., 2017; Masi et al., 2017). These confounds (Rao et al., 2017; Brown et al., 2012) may cause models to rely on spurious correlations rather than clinically meaningful measures (Ferrari et al., 2020).

Numerous computer-aided diagnosis methods have been developed based on FC analysis for diagnosing neurological disorders. Among these, graph neural networks (GNNs) have become a dominant approach owing to their powerful graph embedding capabilities. Building on this strength, recent works (Scarselli et al., 2008) and (Cui et al., 2022) have demonstrated the effectiveness of GNNs in analyzing both brain networks and population networks. However, two main limitations exist in current brain network GNNs: (1) the underutilization of essential information encoded in brain atlases, and (2) the sole focus on individual FC embeddings, neglecting the inter-individual relationships both within and across groups (Wang et al., 2024b). Although the population GNNs incorporate non-imaging data to model relationships between subjects, they often rely on linking individuals from the same sites or with similar demographics (Huang and Chung, 2020; Zhang et al., 2023a). Given that GNNs operate through neighborhood aggregation (Chen et al., 2024a), this approach amplifies the biases inherent in FC data, where confounding factors such as site and demographic variations already mask disease-relevant patterns.

---

\*Corresponding authors: dyao@uestc.edu.cn (Dezhong Yao) and dqguo@uestc.edu.cn (Daqing Guo).

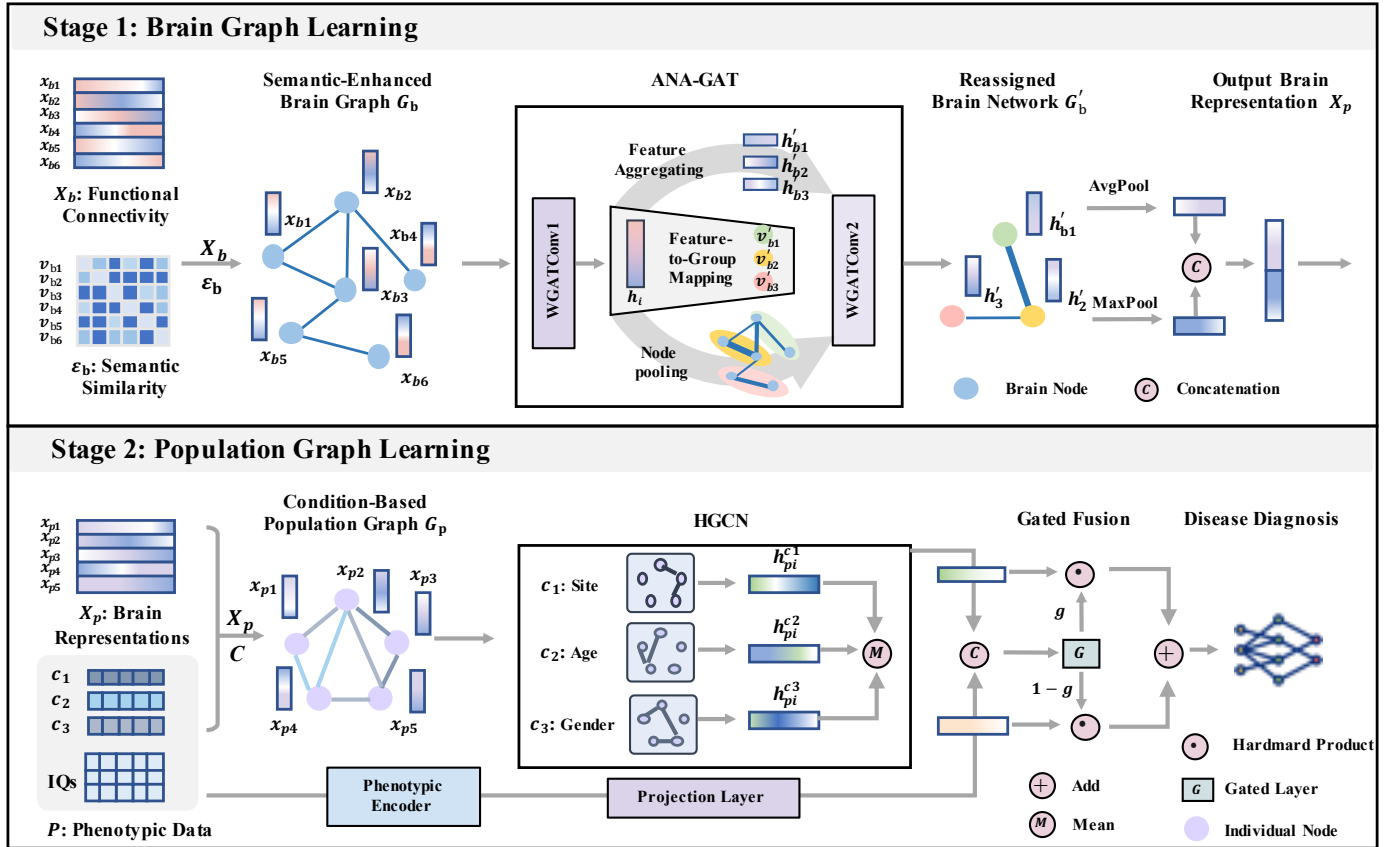


Figure 1: The framework of our proposed Brain-to-Population Graph Learning Network. The upper section depicts the first stage, which constructs semantic-enhanced brain graphs and learns brain representations using Adaptive Node Reassignment Graph Attention Network (ANR-GAT). The lower section illustrates the second stage, building a condition-based population graph and capturing meaningful patterns via a Heterogeneous Graph Convolutional Network (HGNC) and a gated fusion mechanism to integrate phenotypic data.

Moreover, despite the critical biological insights encoded in brain atlases, their potential remains underutilized due to the absence of methods for extracting interpretable and computationally efficient representations, coupled with the need for standardized and precise descriptions of brain regions. Recent advances in large language models (LLMs) have demonstrated promise in medical and neuroscience applications, offering potential solutions to bridge this gap (Achiam et al., 2023). These models can distill vast knowledge repositories into compact representations, serving as robust foundations for downstream tasks (Bzdok et al., 2024). Textual descriptions can additionally be encoded into high-dimensional vectors via embedding models, effectively capturing contextual relationships (Jain and Chadha, 2021). Therefore, LLMs have been successfully deployed to generate precise explanations of medical concepts (Yan et al., 2023) and compute semantic similarities between them (Peng et al., 2024). However, their direct application to information in the brain region remains largely unexplored.

To address these aforementioned challenges, we propose a novel two-stage Brain-to-Population Graph Learning (B2P-GL) framework. In the first stage, termed brain representation learning, we leverage GPT-4 and the embedding model to construct a semantic-enhanced brain graph by calculating semantic similarities between brain regions. The graph is refined using the

Adaptive Node Reassignment Graph Attention Network (ANR-GAT), which captures latent node relationships while improving the interpretability of the brain network. In the second stage, termed population disorder diagnosis, we construct a condition-based heterogeneous graph by connecting nodes with high similarity in brain features but different categories within one condition. This structure enables a Heterogeneous Graph Convolutional Network (HGNC) to aggregate cross-condition messages while mitigating confounding effects. We further integrate phenotypic data via gated fusion to boost diagnostic accuracy. The proposed framework is validated on three large-scale, publicly available brain disorder datasets (ABIDE I, ADHD-200, and Rest-meta-MDD), evaluating both the ANR-GAT model and the B2P-GL framework to ensure adaptability across broader applications.

The main contributions of B2P-GL are as follows:

- We propose the B2P-GL framework, which integrates a two-stage GNN to learn brain representations and population-level interactions, thereby improving both neuroscientific interpretability and diagnostic performance.
- We introduce semantic brain region embeddings and adaptive node reassignment for richer brain graph representations, and a condition-based population graph leveraging

phenotypic data to reduce confounding and guide HGCN toward disorder-relevant patterns.

- We evaluate the proposed B2P-GL framework on three publicly available brain disorder datasets. Experimental results demonstrate that B2P-GL outperforms existing baselines, indicating its effectiveness and generalizability across diverse diagnostic tasks.

## 2. Related Work

### 2.1. GNN-based Neurological Disorders Diagnosis

Computer-aided diagnosis using resting-state functional MRI (rs-fMRI) data has gained increasing interest, with approaches ranging from traditional machine learning methods like support vector machines (Gallo et al., 2023) to deep learning techniques such as convolutional neural networks (Huang et al., 2023), autoencoders (Yin et al., 2021), and transformers (Kan et al., 2022; Bannadabhavi et al., 2023). Among these, GNN has emerged as a powerful framework for modeling brain networks (Li et al., 2019) and population networks (Cao et al., 2021), due to their graph embedding capabilities and interpretability (Li et al., 2019; Qin et al., 2022).

Researchers have explored multi-view FC across different atlases (Wang et al., 2024b), multi-modal MRI data (Chen et al., 2022b; Zhu et al., 2022), and dynamic FC (Campbell et al., 2023) to enrich FC representations in brain networks. However, these methods often require additional modalities or costly pre-processing. To improve brain network representation, advanced graph structures like hypergraphs (Ji et al., 2022; Zuo et al., 2024) and heterogeneous graphs (Wen et al., 2024), as well as learning methods such as metric learning (Ktena et al., 2018), contrastive learning (Zhang et al., 2023b; Wang et al., 2025), and adversarial learning (Chen et al., 2022b; Zuo et al., 2024), have been applied to capture key patterns in FC data. In our brain representation learning, we enhance brain network representation by leveraging large language models (LLMs) to extract rich textual descriptions of brain regions, encoding their functional and structural characteristics. These embeddings provide additional semantic information, enriching the graph representations in brain network analysis.

In population networks, neurological disorder prediction is treated as a node classification task. Node features are derived from the upper triangle of FC matrices (Shao et al., 2023) or extracted using methods like recursive feature elimination (RFE) (Yang et al., 2023). Alternatively, GNNs are employed to learn graph representations of FC for node feature embedding (Jiang et al., 2020; Zhang et al., 2023a). Non-imaging data, such as phenotypic features, are integrated by mapping them to edge weights (Huang and Chung, 2020; Zhang et al., 2023a) or learning modality-shared and modality-specific representations to construct population networks (Zheng et al., 2022; Chen et al., 2024b). While some recent studies have explored jointly modeling brain-level and population-level graphs to capture both within- and between-subject patterns (Pan et al., 2022; Li and Zhang, 2024; Zeng et al., 2025), we use a two-stage approach to

help disentangle subject-specific neural features from broader population-level variations.

### 2.2. Neurological Disorders with Large Language Models

Recent studies have explored LLMs in medical AI, particularly for tasks like medical image segmentation (Huang et al., 2024; Zhang et al., 2023c), using region-based prompts to identify regions of interest (ROIs). In neurological disorder diagnosis, MMGPL (Peng et al., 2024) employs concept learning to filter irrelevant tokens by measuring semantic similarity to disease-related concepts. Moreover, fTSP (Wang et al., 2024a) leverages pre-trained vision-language models to enhance brain analysis, generating instance-level textual descriptions for each fMRI scan. While these methods demonstrate the effectiveness of LLMs in learning token-level or instance-level knowledge, the direct modeling of brain region semantics has received limited attention. To address this gap, we utilize LLMs to encode brain regions’ textual descriptions, capturing their functional and structural characteristics. By computing semantic embeddings, we measure the similarity between brain regions based on their functional and structural profiles. This approach identifies connectivity patterns and coherence among regions with shared roles, offering new insights into brain network organization.

## 3. Preliminary

### 3.1. Weighted Graph Attention in Brain Network

Let  $\mathcal{G}_b = (\mathcal{V}_b, \mathcal{E}_b, \mathbf{X}_b, \mathbf{W}_b)$  denote the brain network, where  $\mathcal{V}_b$  denotes the set of brain nodes,  $\mathcal{E}_b \subseteq \mathcal{V}_b \times \mathcal{V}_b$  is the set of edges between brain nodes,  $\mathbf{X}_b \in \mathbb{R}^{|\mathcal{V}_b| \times F}$  is the node feature matrix with  $F$  denoting the feature dimension.  $\mathbf{W}_b \in \mathbb{R}^{|\mathcal{V}_b| \times |\mathcal{V}_b|}$  encodes the pairwise edge weights between nodes.

Graph Attention Network (GAT) employs a self-attention mechanism to dynamically learn the attention scores between neighboring brain nodes (Ye and Ji, 2021). At layer  $l$ , the feature of brain node  $i$  is denoted as  $\mathbf{h}_{bi}^{(l)} \in \mathbb{R}^F$ , and is first linearly transformed by a learnable weight matrix  $\mathbf{W}^{(l)} \in \mathbb{R}^{F \times F}$  to obtain:  $\mathbf{z}_i^{(l)} = \mathbf{W}^{(l)} \mathbf{h}_{bi}^{(l)}$ , where  $\mathbf{W}^{(l)} \in \mathbb{R}^{F \times F}$  is a learnable weight matrix, and  $F'$  is the dimensionality of the transformed features. The attention score  $e_{ij}$  between nodes  $i$  and  $j$  is computed as:  $e_{ij} = \text{LeakyReLU}(\mathbf{a}^\top [\mathbf{z}_i^{(l)} \parallel \mathbf{z}_j^{(l)}])$ , where  $\mathbf{a} \in \mathbb{R}^{2F'}$  is a learnable parameter vector, and  $\parallel$  denotes concatenation. Here,  $\mathbf{z}_i^{(l)} \parallel \mathbf{z}_j^{(l)} \in \mathbb{R}^{2F'}$  is the concatenated feature vector of brain nodes  $i$  and  $j$ .

To better incorporate the original edge weight information, we scale the attention score as:  $\tilde{e}_{ij} = w_{ij} \cdot e_{ij}$ , where  $w_{ij} \in \mathbb{R}$  represents the original normalized relation weight. We refer to this approach as the weighted graph attention network (WGAT) in later sections for brain representation learning. Finally, the updated feature for brain node  $i$  at layer  $l + 1$ ,  $\mathbf{h}_{bi}^{(l+1)} \in \mathbb{R}^{F'}$  is computed as:

$$\mathbf{h}_{bi}^{(l+1)} = \sigma \left( \sum_{j \in \mathcal{N}(i)} \frac{\exp(\tilde{e}_{ij})}{\sum_{k \in \mathcal{N}(i)} \exp(\tilde{e}_{ik})} \mathbf{z}_j^{(l)} \right) \quad (1)$$

where the sum is taken over the brain node neighbors  $\mathcal{N}_b(i)$ , and  $\sigma$  is a non-linear activation function. The output  $\mathbf{h}_{bi}^{(l+1)} \in \mathbb{R}^{F'}$  represents the feature vector for node  $i$  at layer  $l + 1$ .

### 3.2. Heterogeneous Graph Convolution in Population Network

The population graph is defined as  $G_p = (\mathcal{V}_p, \mathcal{E}_p, \mathbf{X}_p, \mathcal{C})$ , where  $\mathcal{V}_p$  represents individual nodes,  $\mathcal{E}_p$  represents population edges,  $\mathbf{X}_p \in \mathbb{R}^{|\mathcal{V}_p| \times F_2}$  is the node feature matrix with  $F_2$  denoting the feature dimension and  $\mathcal{C}$  is a set of conditions that define the relationships between nodes. A heterogeneous graph network (HGCN) (Schlichtkrull et al., 2018; Zhang et al., 2019) is used to propagate information across different relations. Each edge corresponds to a unique relationship under a specific condition  $c \in \mathcal{C}$ .

For individual node  $i$ , its feature representation  $\mathbf{h}_{pi}^c \in \mathbb{R}^{F'_2}$  is updated by aggregating features from its condition-specific neighbors  $\mathcal{N}_p(i)^c$ , using a learnable weight matrix  $W^c \in \mathbb{R}^{F'_2 \times F'_2}$  specific to condition  $c$ . HGCN ensures that the aggregation reflects the unique relational patterns within each condition. The final feature representation  $\mathbf{h}_{pi} \in \mathbb{R}^{F'_2}$  is computed by mean aggregation across all conditions:

$$\mathbf{h}_{pi} = \sigma \left( \frac{1}{|\mathcal{C}|} \sum_{c \in \mathcal{C}} \sum_{j \in \mathcal{N}_p(i)^c} \frac{1}{|\mathcal{N}_p(i)^c|} W^c \mathbf{h}_{pj} \right), \quad (2)$$

where  $\sigma$  is a non-linear activation function, and  $\mathcal{N}_p(i)^c$  denotes the neighbors of individual node  $v$  under condition  $c$ .

## 4. Method

The Brain-to-Population Graph Learning framework, as illustrated in Figure 1, uses a two-stage GNN approach to combine individual brain connectivity analysis with population insights. In the first stage, we model semantic-enhanced brain graphs using the ANR-GAT for brain representation learning (Section 4.1). In the second stage, we construct condition-based population graphs and leverage HGCN with gated fusion to incorporate phenotypic data for disease diagnosis (Section 4.2).

### 4.1. Brain Representation Learning

As defined in Section 3.1, let  $\mathcal{G}_b = (\mathcal{V}_b, \mathcal{E}_b, \mathbf{X}_b, \mathbf{W}_b)$  denote the brain graph, where brain nodes  $\mathcal{V}_b$  correspond to parcellated regions of interest (ROIs) based on a brain atlas, and edges  $\mathcal{E}_b$  capture the semantic relationships with weight  $\mathbf{W}_b$ , reflecting functional and structural connections between the atlas regions. This forms a semantic-enhanced brain graph. Each node  $i$  has a feature vector  $\mathbf{X}_{bi} \in \mathbb{R}^F$ , with node features derived from the FC matrix, calculated using Pearson Correlation (Cohen et al., 2009), where each row represents the correlation coefficient between a node with all other nodes.

#### 4.1.1. Semantic-Enhanced Brain Graph

A common approach in healthcare involves consulting experts. However, recent advancements in instruction-following large language models, like GPT-4 (Achiam et al., 2023), offer

a promising alternative for addressing language-related challenges in the medical field (Nori et al., 2023). By instructing GPT-4 with targeted prompts, we can generate lists of concepts linked to specific conditions, reducing annotation costs and utilizing large language models to tap into extensive medical knowledge (Peng et al., 2024).

In this work, we leverage large language models (LLMs) to derive semantic embeddings of brain regions, capturing both their functional roles and structural properties. For each brain region, prompts are constructed to elicit descriptive text capturing its core neurobiological attributes. These responses are then tokenized and embedded using the text encoder. An illustration of this process is provided in Figure 2. To quantify the semantic relationships between regions, we compute pairwise cosine similarity between their embeddings:  $\text{Sim}(u, v) = \frac{\mathbf{s}_u \cdot \mathbf{s}_v}{\|\mathbf{s}_u\| \|\mathbf{s}_v\|}$ , where  $\mathbf{s}_u$  and  $\mathbf{s}_v$ , where  $\mathbf{s}_u$  and  $\mathbf{s}_v$  denote the semantic embeddings of brain regions  $u$  and  $v$ , respectively. Based on these similarity scores, we construct edges in the brain graph, using a thresholded similarity score as the edge weight. This incorporation of semantic similarity enables the graph structure to more faithfully reflect the functional and structural relevance between regions.

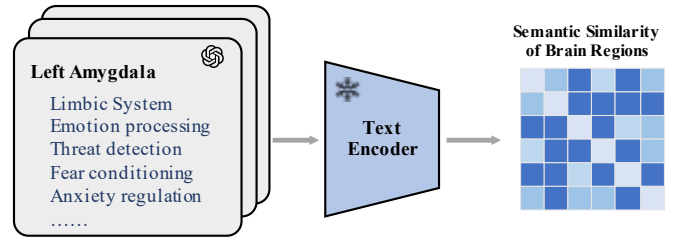


Figure 2: Illustration of semantic similarity generation for brain regions. Functional and structural descriptions (e.g., for the left amygdala) are encoded using a text encoder to produce embeddings. These embeddings are then used to compute semantic similarity between regions.

To ensure consistency and reproducibility in concept generation, we designed a structured prompt format rooted in established neuroscience standards, such as the Terminologia Neuroanatomica and the Human Connectome Project. The schema guiding the initial neuroanatomical descriptions is illustrated in Figure 3.

To further enhance the granularity and generalizability of the extracted features, we introduce a secondary prompt tailored to extract hierarchical, ontology-driven concepts for each brain region. This prompt guides the model to produce fine-grained annotations that align with known structural-functional hierarchies. An overview of this concept extraction process is shown in Figure 4.

In the ANR-GAT, meaningful features are extracted from neighboring nodes using WGAT, while feature-to-group mapping captures latent relationships between nodes to reassign the graph. Finally, brain representations are summarized using max and mean pooling across all nodes.

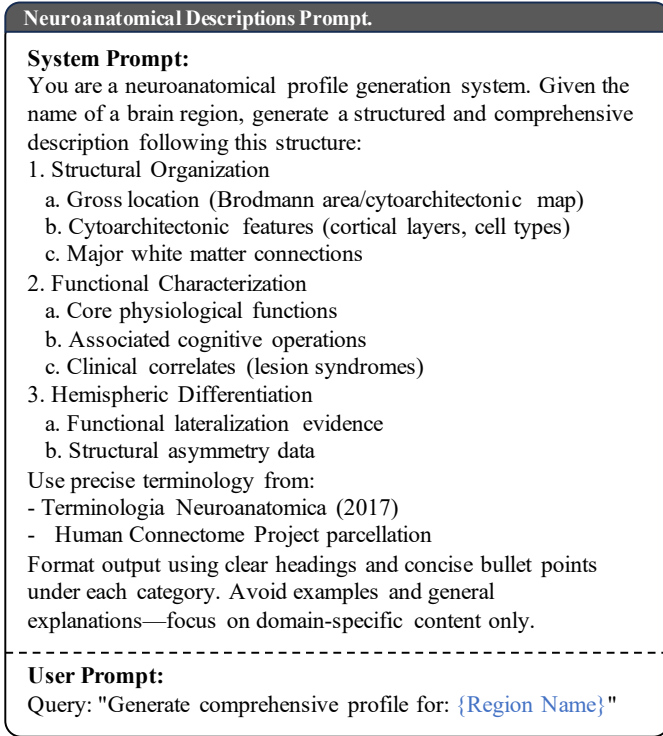


Figure 3: Prompt for generating neuroanatomical descriptions.

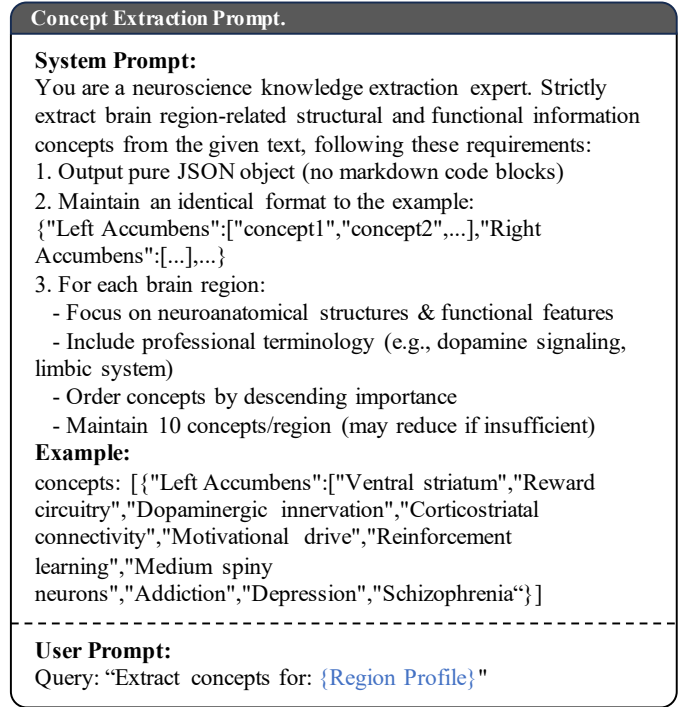


Figure 4: Prompt for structured extraction of neuroanatomical and functional concepts from text.

#### 4.1.2. Feature-to-Group Mapping

As part of the ANR-GAT model, the node feature matrix  $\mathbf{H}_b \in \mathbb{R}^{V_b \times F}$  is obtained after the WGAT layer. To reassign nodes into new groups based on their feature representations, we introduce a feature-to-group mapping mechanism that projects these features into a shared group space. The group assignment matrix  $\mathbf{M} \in \mathbb{R}^{V_b \times N_g}$ , where  $N_g$  is the number of groups, is computed by applying a learnable reassignment weight matrix  $\mathbf{W}_r \in \mathbb{R}^{F \times N_g}$  followed by a softmax operation:  $\mathbf{M} = \text{Softmax}(\mathbf{H}_b \mathbf{W}_r)$ , where the softmax is applied row-wise to ensure that the group assignment probabilities for each node sum to one.

For each node  $i \in \mathcal{V}$ , the group assignment  $\text{group}_i$  is determined by selecting the group with the highest probability from  $\mathbf{M}$  along the group dimension:  $\text{group}_i = \arg \max_j M_{ij}$ ,  $\forall j \in \{1, 2, \dots, N_g\}$ . As illustrated in Figure 1, this mapping is a key component of the ANR-GAT model, designed for brain graph representation learning. Node features are aggregated within each group, combining information from nodes reassigned to the same group. The edges are also remapped between groups, guided by the original graph connectivity and the reassigned groups. This process simplifies the graph structure while preserving key relationships, enabling the generation of new node representations that are passed to subsequent layers of WGAT for further processing. As an intermediate step bridging the WGAT layers, the feature-to-group mapping facilitates hierarchical feature learning and graph structure simplification.

#### 4.2. Population Disease Diagnosis

As defined in Section 3.2, let  $G_p = (\mathcal{V}_p, \mathcal{E}_p, \mathbf{X}_p, C)$ , denote the condition-based population graph, where individual node features  $\mathbf{X}_p$  represent brain representations from the first stage, and edges  $\mathcal{E}_p$  are constructed based on the condition set  $C$  with node feature similarities to reduce biases while highlighting disease-specific patterns. We employ HGCN to capture key features within the population and use gated fusion to incorporate phenotypic features for enhanced diagnosis.

##### 4.2.1. Condition-Based Population Graph

Given the heterogeneous nature of biomedical data, non-imaging variables or confounds (Rao et al., 2017) can influence imaging data but may not be clinically relevant (Brown et al., 2012). These confounds introduce ambiguity in identifying the true predictive sources, potentially leading models to rely on confounds instead of the target measure (Ferrari et al., 2020). Unlike traditional approaches that directly connect nodes within the same category of a condition, our method leverages cross-category feature similarities to mitigate phenotype or site-related biases. This guides the model in learning intrinsic, disease-specific patterns rather than artifacts introduced by external conditions. To quantify the similarity of node features, we compute a scaled adjacency matrix  $A$ , derived from the pairwise feature distances and a Gaussian kernel:  $A_{ij} = \exp\left(-\frac{\|\mathbf{h}_{pi} - \mathbf{h}_{pj}\|^2}{2\sigma^2}\right)$ , where  $\mathbf{h}_{pi}$  and  $\mathbf{h}_{pj}$  are the feature vectors of nodes  $i$  and  $j$ , and  $\sigma$  is a scaling parameter controlling the kernel width. Let  $A^c$  denote the adjacency matrix for distinct categories within condition  $c$ , the entry  $a_{ij}$  is defined

as:  $a_{ij}^c = \mathbb{I}(c_i \neq c_j)$ , where  $\mathbb{I}$  is the indicator function, equal to 1 if  $c_i \neq c_j$  and 0 otherwise. Based on  $A^c$ , we select the top- $k$  most similar nodes to construct the overall condition-related edge index, minimizing biases for graph learning.

The resulting population graph is trained using a heterogeneous GCN (HGCN) that is aware of condition types. HGCN assigns distinct transformation weights to different edge types, enabling the model to disentangle the effects of confounds and more effectively capture disease-relevant signals.

#### 4.2.2. Gated Fusion With Phenotypic Data

The gated fusion mechanism adaptively combines graph-derived node features with encoded phenotypic features, ensuring that the final representation effectively integrates multimodal information while preserving the contributions of each source. Let  $\mathbf{H}_p \in \mathbb{R}^{|\mathcal{V}_p| \times F_2}$  denote the graph node features and  $\mathbf{P} \in \mathbb{R}^{|\mathcal{V}_p| \times D_p}$  represent the phenotypic features, where  $|\mathcal{V}_p|$  is the number of individual nodes,  $F_2$  is the dimension of the individual node features after the HGCN, and  $D_p$  is the dimension of the phenotypic data. Phenotypic features are transformed into  $\mathbf{P}' \in \mathbb{R}^{|\mathcal{V}_p| \times F_2}$  through a learnable network that maps  $\mathbf{P}$  to the same dimensionality as  $\mathbf{H}_b$ . The concatenation of  $\mathbf{H}_b$  and  $\mathbf{P}'$  passes through a linear layer followed by a sigmoid activation to produce the gating coefficient  $\mathbf{g}$ :

$$\mathbf{g} = \sigma(W_{\text{gate}} \cdot [\mathbf{H}_b, \mathbf{P}'] + b_{\text{gate}}), \quad (3)$$

where  $W_{\text{gate}}$  and  $b_{\text{gate}}$  are the learnable weights and biases of the gating layer. The final representation is computed as a weighted combination of  $\mathbf{H}_b$  and  $\mathbf{P}'$ , modulated by  $\mathbf{g}$ :

$$\hat{\mathbf{H}}_b = \text{LayerNorm}(\text{ReLU}(\mathbf{g} \odot \mathbf{H}_b + (1 - \mathbf{g}) \odot \mathbf{P}')), \quad (4)$$

where  $\odot$  denotes element-wise multiplication. This mechanism enables dynamic integration of graph-derived and phenotypic information, enhancing the expressiveness and adaptability of the model.

### 4.3. Two-Stage Optimization for B2P-GL Framework

The proposed framework is comprised of two stages. The first stage is devoted to optimizing the representation of the brain graph, while the second stage aims to enhance the classification of disorders.

In brain graph learning, we formulate optimization as a joint problem that simultaneously learns node representations and enhances classification accuracy. Accordingly, the objective is to minimize a combined loss:  $\mathcal{L}_1 = \mathcal{L}_{\text{cls}} + \mathcal{L}_{\text{sim}}$ , where  $\mathcal{L}_{\text{cls}}$  is the classification loss and  $\mathcal{L}_{\text{sim}}$  is the similarity loss. This optimization enables the model to learn effective node embeddings while enhancing classification performance.

The classification loss is computed using cross-entropy:  $\mathcal{L}_{\text{cls}} = -\frac{1}{N} \sum_{i=1}^N \sum_{c=1}^C y_{i,c} \log \hat{y}_{i,c}$ , where  $\mathbf{y}$  represents the ground truth labels and  $\hat{\mathbf{y}}$  denotes the predictions.

#### 4.3.1. Similarity Loss

The similarity loss aligns feature similarities with label similarities. Let  $\mathbf{H} \in \mathbb{R}^{N \times d}$  represent node embeddings, with pairwise similarity defined as:  $S_{i,j} = \frac{\mathbf{h}_i \cdot \mathbf{h}_j}{\sqrt{d}}$ . Row-normalizing  $\mathbf{S}$  with

the softmax function produces the normalized similarity matrix  $\mathbf{S}'$ . The loss is:

$$\mathcal{L}_{\text{sim}} = \frac{1}{N^2} \|\mathbf{S}' - \mathbb{I}[y_i = y_j]\|_F^2, \quad (5)$$

where  $\mathbb{I}[y_i = y_j]$  equals 1 if labels match and 0 otherwise. This loss encourages embeddings of nodes with the same label to be closer with different labels to be farther apart.

#### 4.3.2. Gradient of Similarity Matrix.

The gradient of  $\mathcal{L}_{\text{sim}}$  adjusts embeddings based on similarity alignment. For node  $i$ :

$$\begin{aligned} \frac{\partial \mathcal{L}_{\text{sim}}}{\partial \mathbf{h}_i} &= \frac{2}{N^2 \sqrt{d}} \sum_{j=1}^N (\mathbf{S}'_{i,j} - \mathbb{I}[y_i = y_j]) \mathbf{S}'_{i,j} \\ &\quad \times \left( \mathbf{h}_j - \sum_{k=1}^N \mathbf{S}'_{i,k} \mathbf{h}_k \right). \end{aligned} \quad (6)$$

For the same label  $\mathbb{I}[y_i = y_j] = 1$ , the gradient pulls embeddings closer while the gradient pushes embeddings apart when  $\mathbb{I}[y_i = y_j] = 0$ .

#### 4.3.3. Compatibility of the Gaussian Kernel Similarity

In the second stage, we construct the population graph by using the Gaussian kernel similarity measurement, which can be rewritten in terms of the dot product:

$$\begin{aligned} K(\mathbf{h}_i, \mathbf{h}_j) &= \exp\left(-\frac{2(1 - \mathbf{h}_i \cdot \mathbf{h}_j)}{2\sigma^2}\right) \\ &= \exp\left(\frac{\mathbf{h}_i \cdot \mathbf{h}_j}{\sigma^2}\right) \cdot C, \end{aligned} \quad (7)$$

where  $C = \exp(-1/\sigma^2)$  is a constant. This shows that maximizing  $\mathbf{h}_i \cdot \mathbf{h}_j$  also maximizes the kernel similarity for same-class pairs. The embeddings trained with  $\mathcal{L}_{\text{sim}}$  inherently optimize dot-product similarities, which are directly compatible with the Gaussian kernel.

Considering the integration of the phenotypic, population graph learning extends the optimization from brain graph learning by independently aligning brain and phenotypic representations with label similarities while combining them with classification losses. The total loss function is  $\mathcal{L}_2 = \mathcal{L}_{\text{sim2}} + \mathcal{L}_{\text{cls}}$ , where  $\mathcal{L}_{\text{sim2}}$  loss consists of a node representation similarity loss and a phenotypic fusion similarity loss, where the former ensures brain features capture disorder-relevant patterns, the latter aligns multimodal features with label similarities without enforcing consistency with the original brain features. This approach enables complementary learning of disease-related patterns from both modalities, enhancing predictive performance while preserving their unique contributions.

## 5. Experiments

In this section, we first provide a comprehensive overview of the experimental settings, including details on the publicly

available preprocessed datasets, evaluation metrics, and implementation configurations. We then present extensive experiments to validate the effectiveness of the proposed framework and its individual components in two stages. The results demonstrate that B2P-GL achieves strong performance across three brain disorder datasets. Furthermore, ablation studies are conducted to examine the contribution of each module within the framework. Finally, we perform an interpretability analysis to explore clinically relevant patterns associated with different brain disorders.

### 5.1. Datasets

We evaluate our method on three widely used neuroimaging datasets related to neurodevelopmental and psychiatric disorders: Autism Brain Imaging Data Exchange I (ABIDE I)(Di Martino et al., 2014), Attention Deficit Hyperactivity Disorder-200 (ADHD-200)(Milham et al., 2012), and REST-meta-MDD (Chen et al., 2022a).

The ABIDE I is a publicly available, multi-site dataset comprising resting-state functional magnetic resonance imaging (rs-fMRI) data (Di Martino et al., 2014). It includes individuals diagnosed with Autism Spectrum Disorder (ASD) and normal controls (NC). Preprocessing was performed using the Configurable Pipeline for the Analysis of Connectomes (CPAC) (Craddock et al., 2013). Key preprocessing steps included band-pass filtering, global signal regression, and spatial normalization to a standard atlas.

The ADHD-200 dataset includes rs-fMRI scans from children and adolescents diagnosed with Attention-Deficit/Hyperactivity Disorder (ADHD) as well as typically developing controls (TDC). Preprocessing followed the Athena pipeline (Bellec et al., 2017), which included normalization to MNI space, nuisance regression, temporal filtering, and spatial smoothing. We further incorporated labeled test data from the ADHD-200 Global Competition to expand the dataset.

The REST-meta-MDD dataset, released by the Depression Imaging REsearch (DIRECT) consortium, aggregates rs-fMRI data from 25 research groups across 17 hospitals in China (Chen et al., 2022a). The dataset contains both patients diagnosed with Major Depressive Disorder (MDD) and demographically matched healthy controls (NC). All imaging data were preprocessed using the standardized Data Processing Assistant for Resting-State fMRI (DPARSF) pipeline. Following previously established criteria, we excluded subjects with incomplete phenotypic records, poor spatial normalization, excessive head motion, or from sites with fewer than 10 participants per group (Yan et al., 2019).

Table 1 summarizes the demographic characteristics of the three datasets. ADHD-200 primarily includes children and adolescents, whereas ABIDE I and REST-meta-MDD cover a broader age range extending into adulthood. ABIDE I and ADHD-200 show a clear male predominance, while REST-meta-MDD has a more balanced gender distribution. All datasets are collected from multiple sites, contributing to demographic and acquisition variability. ABIDE I includes 850 participants from 20 sites, ADHD-200 consists of 938 participants from 7 sites, and the REST-meta-MDD comprises 1,567

participants across 16 sites. Both ABIDE I and ADHD-200 provide Full-Scale, Performance, and Verbal IQ scores, although a substantial portion of these values are missing in ABIDE I and ADHD-200 datasets. REST-meta-MDD includes years of education, which may serve as a proxy for cognitive and socioeconomic background.

Table 1: Participant Demographics and Dataset Statistics for ABIDE I, ADHD-200 and Rest-meta-MDD

| Dataset          | ABIDE             | ADHD200             | Rest-meta-MDD     |
|------------------|-------------------|---------------------|-------------------|
| Participants     | ASD: 396, NC: 454 | ADHD: 450, TDC: 488 | MDD: 814, NC: 753 |
| Gender           | M: 711, F: 139    | M: 588, F: 350      | M: 605, F: 962    |
| Sites            | 20                | 7                   | 16                |
| Age (years)      | 6.47 - 58.0       | 7.09 - 26.31        | 18.0 - 65.0       |
| Education(years) | -                 | -                   | 3.0- 23.0         |
| IQ               | FIQ, PIQ, VIQ     | FIQ, PIQ, VIQ       | -                 |

### 5.2. Experimental Settings

All experiments were conducted using 5 repetitions of 10-fold cross-validation to ensure robustness. Model performance was assessed using four commonly employed metrics: accuracy (ACC), area under the curve (AUC), specificity (SPE), and sensitivity (SEN).

Models were implemented and evaluated within a PyTorch environment using an A800 GPU. Table 2 summarizes the hyperparameter configurations for the two stages of the B2P-GL model across the ABIDE I, ADHD-200, and REST-meta-MDD datasets. The first stage adopts the ANR-GAT architecture, while the second stage is based on the HGCN framework. The table outlines dataset-specific settings for each stage, including the optimizer, learning rate, batch size, number of training epochs, hidden dimensions, and selected phenotypic variables.

Table 2: Model configuration and hyperparameters across different datasets

| Parameters          | ABIDE I               | ADHD-200              | Rest-meta-MDD         |
|---------------------|-----------------------|-----------------------|-----------------------|
| <b>Stage 1</b>      |                       |                       |                       |
| optimizer           | Adam                  | Adam                  | Adam                  |
| learning rate       | $1.00 \times 10^{-4}$ | $1.00 \times 10^{-4}$ | $1.00 \times 10^{-4}$ |
| number of epoch     | 200                   | 200                   | 200                   |
| batch size          | 32                    | 32                    | 32                    |
| hidden channel      | 512                   | 256                   | 512                   |
| threshold           | 0.6                   | 0.5                   | 0.6                   |
| group number        | 60                    | 50                    | 60                    |
| <b>Stage 2</b>      |                       |                       |                       |
| optimizer           | AdamW                 | AdamW                 | AdamW                 |
| learning rate       | $1.00 \times 10^{-2}$ | $1.00 \times 10^{-2}$ | $1.00 \times 10^{-2}$ |
| weight decay        | $5.00 \times 10^{-5}$ | $5.00 \times 10^{-5}$ | $5.00 \times 10^{-5}$ |
| number of epoch     | 100                   | 100                   | 100                   |
| hidden channel      | 128                   | 128                   | 128                   |
| top-k               | 5                     | 4                     | 4                     |
| condition selection | site, gender, age     | site, gender          | site, gender          |
| phenotype selection | site, gender, age, IQ | site, IQ              | site, education       |

### 5.3. Quantitative Comparison of Model Performance

To comprehensively assess the performance of our proposed models, we conducted a systematic comparison across three major types of architectures: (1) non-graph neural networks, which treat the FC matrix as an image input; (2) graph classification models, which operate on individual-level FC graphs;

Table 3: Performance comparison of graph-based and non-graph models across multiple datasets. Models are divided into three categories: (1) non-graph neural networks, (2) graph classification using FC, and (3) node classification with phenotypic data. Proposed methods include ANR-GAT and B2P-GL. Best results per metric and dataset are bolded.

| Model                              | ABIDE I                          |                                  |                                  |                                  | ADHD-200                         |                                  |                                  |                                  | REST-meta-MDD                    |                                  |                                  |                                  |
|------------------------------------|----------------------------------|----------------------------------|----------------------------------|----------------------------------|----------------------------------|----------------------------------|----------------------------------|----------------------------------|----------------------------------|----------------------------------|----------------------------------|----------------------------------|
|                                    | ACC<br>(%, $\uparrow$ )          | AUC<br>(%, $\uparrow$ )          | SPE<br>(%, $\uparrow$ )          | SEN<br>(%, $\uparrow$ )          | ACC<br>(%, $\uparrow$ )          | AUC<br>(%, $\uparrow$ )          | SPE<br>(%, $\uparrow$ )          | SEN<br>(%, $\uparrow$ )          | ACC<br>(%, $\uparrow$ )          | AUC<br>(%, $\uparrow$ )          | SPE<br>(%, $\uparrow$ )          | SEN<br>(%, $\uparrow$ )          |
| <b>Non-Graph Neural Networks</b>   |                                  |                                  |                                  |                                  |                                  |                                  |                                  |                                  |                                  |                                  |                                  |                                  |
| ViT                                | 66.8 $\pm$ 1.4                   | 66.2 $\pm$ 1.7                   | 74.5 $\pm$ 3.9                   | 58.0 $\pm$ 6.5                   | 68.3 $\pm$ 0.7                   | 62.8 $\pm$ 1.6                   | 85.6 $\pm$ 2.2                   | 40.0 $\pm$ 5.3                   | 63.8 $\pm$ 0.5                   | 63.6 $\pm$ 0.6                   | 57.4 $\pm$ 4.8                   | 69.7 $\pm$ 3.9                   |
| CNN                                | 69.0 $\pm$ 0.5                   | 68.7 $\pm$ 0.4                   | 72.0 $\pm$ 4.6                   | 65.5 $\pm$ 4.7                   | 66.0 $\pm$ 0.5                   | 58.1 $\pm$ 1.1                   | 91.1 $\pm$ 1.7                   | 25.1 $\pm$ 3.7                   | 65.1 $\pm$ 1.5                   | 65.1 $\pm$ 1.4                   | 63.8 $\pm$ 3.2                   | 66.3 $\pm$ 5.3                   |
| BrainNetCNN                        | <b>72.2 <math>\pm</math> 1.1</b> | <b>72.0 <math>\pm</math> 1.3</b> | <b>74.9 <math>\pm</math> 2.1</b> | <b>69.1 <math>\pm</math> 4.2</b> | 66.3 $\pm$ 0.6                   | 59.6 $\pm$ 1.5                   | <b>87.8 <math>\pm</math> 2.3</b> | 31.3 $\pm$ 5.3                   | <b>66.6 <math>\pm</math> 1.0</b> | <b>66.6 <math>\pm</math> 1.0</b> | <b>66.1 <math>\pm</math> 2.2</b> | <b>67.1 <math>\pm</math> 2.7</b> |
| BrainNetTransformer                | 69.5 $\pm$ 0.1                   | 69.1 $\pm$ 0.3                   | 73.7 $\pm$ 1.4                   | 64.5 $\pm$ 2.1                   | <b>68.7 <math>\pm</math> 0.3</b> | <b>64.1 <math>\pm</math> 1.0</b> | 83.2 $\pm$ 1.8                   | <b>45.0 <math>\pm</math> 3.7</b> | 63.9 $\pm$ 0.1                   | 63.8 $\pm$ 0.2                   | 60.6 $\pm$ 4.0                   | 67.0 $\pm$ 3.7                   |
| <b>Graph Classification Models</b> |                                  |                                  |                                  |                                  |                                  |                                  |                                  |                                  |                                  |                                  |                                  |                                  |
| GAT                                | 69.7 $\pm$ 0.3                   | 69.1 $\pm$ 0.2                   | 77.5 $\pm$ 1.1                   | 60.8 $\pm$ 0.6                   | 60.1 $\pm$ 0.4                   | 59.8 $\pm$ 0.3                   | <b>66.0 <math>\pm</math> 1.7</b> | 53.6 $\pm$ 0.3                   | 65.1 $\pm$ 0.2                   | 64.9 $\pm$ 0.2                   | 60.3 $\pm$ 0.4                   | 69.4 $\pm$ 0.5                   |
| BrainGNN                           | 67.0 $\pm$ 0.4                   | 65.3 $\pm$ 0.7                   | 74.3 $\pm$ 2.4                   | 56.5 $\pm$ 2.2                   | 61.6 $\pm$ 0.7                   | 60.6 $\pm$ 0.8                   | 61.5 $\pm$ 1.8                   | 61.6 $\pm$ 1.1                   | 64.0 $\pm$ 0.1                   | 65.0 $\pm$ 0.2                   | 64.3 $\pm$ 0.9                   | 63.8 $\pm$ 0.8                   |
| TSEN                               | 70.1 $\pm$ 0.3                   | 69.5 $\pm$ 0.4                   | 79.3 $\pm$ 2.0                   | 59.8 $\pm$ 2.4                   | 62.2 $\pm$ 0.6                   | 62.4 $\pm$ 0.6                   | 57.4 $\pm$ 3.8                   | <b>67.4 <math>\pm</math> 4.1</b> | <b>66.7 <math>\pm</math> 0.7</b> | 66.6 $\pm$ 0.7                   | 66.6 $\pm$ 3.2                   | <b>66.7 <math>\pm</math> 2.8</b> |
| <b>ANR-GAT (ours)</b>              | <b>73.7 <math>\pm</math> 0.6</b> | <b>73.2 <math>\pm</math> 0.6</b> | <b>80.5 <math>\pm</math> 1.8</b> | <b>65.9 <math>\pm</math> 2.1</b> | <b>65.6 <math>\pm</math> 0.6</b> | <b>65.5 <math>\pm</math> 0.6</b> | 64.9 $\pm$ 1.3                   | 63.4 $\pm$ 3.8                   | 66.6 $\pm$ 0.2                   | <b>66.8 <math>\pm</math> 0.2</b> | <b>71.3 <math>\pm</math> 2.0</b> | 62.3 $\pm$ 2.1                   |
| <b>Node Classification Models</b>  |                                  |                                  |                                  |                                  |                                  |                                  |                                  |                                  |                                  |                                  |                                  |                                  |
| Population-GCN                     | 71.1 $\pm$ 0.2                   | 73.9 $\pm$ 0.5                   | 81.3 $\pm$ 0.6                   | 59.3 $\pm$ 0.9                   | 62.9 $\pm$ 1.1                   | 62.6 $\pm$ 2.0                   | 61.6 $\pm$ 3.2                   | 64.1 $\pm$ 1.8                   | 67.2 $\pm$ 0.6                   | 69.4 $\pm$ 0.1                   | 62.3 $\pm$ 2.9                   | 71.8 $\pm$ 1.5                   |
| EV-GCN                             | 71.6 $\pm$ 0.3                   | 72.7 $\pm$ 0.4                   | 78.6 $\pm$ 1.7                   | 63.6 $\pm$ 1.6                   | <b>67.4 <math>\pm</math> 0.1</b> | 66.9 $\pm$ 0.2                   | 68.8 $\pm$ 2.9                   | 66.1 $\pm$ 2.4                   | 66.5 $\pm$ 0.3                   | <b>67.4 <math>\pm</math> 0.4</b> | 60.0 $\pm$ 1.9                   | 72.5 $\pm$ 1.5                   |
| LG-GNN                             | 80.1 $\pm$ 0.8                   | 81.3 $\pm$ 1.2                   | 81.6 $\pm$ 3.0                   | <b>78.8 <math>\pm</math> 2.7</b> | 65.9 $\pm$ 0.9                   | 65.3 $\pm$ 1.6                   | 68.2 $\pm$ 3.0                   | 63.3 $\pm$ 4.1                   | 79.9 $\pm$ 0.4                   | <b>90.6 <math>\pm</math> 0.2</b> | <b>91.2 <math>\pm</math> 0.4</b> | 69.2 $\pm$ 1.1                   |
| <b>B2P-GL (ours)</b>               | <b>83.4 <math>\pm</math> 0.5</b> | <b>83.0 <math>\pm</math> 0.3</b> | <b>88.9 <math>\pm</math> 0.5</b> | 77.1 $\pm$ 0.1                   | <b>78.6 <math>\pm</math> 0.4</b> | <b>78.8 <math>\pm</math> 0.4</b> | <b>82.3 <math>\pm</math> 0.8</b> | <b>75.2 <math>\pm</math> 1.5</b> | <b>82.0 <math>\pm</math> 0.3</b> | 82.0 $\pm$ 0.3                   | 81.3 $\pm$ 1.5                   | <b>82.6 <math>\pm</math> 1.1</b> |

and (3) node classification models, which leverage population graphs constructed from individual embeddings and phenotypic metadata.

For non-graph baselines, we considered four representative architectures: ViT(Dosovitskiy et al., 2020), CNN(Krizhevsky et al., 2017), BrainNetCNN(Kawahara et al., 2017), and BrainNetTransformer(Kan et al., 2022), which directly process FC matrices as images. These models provide a strong baseline for evaluating whether graph structure offers added benefit over traditional 2D processing pipelines.

In the graph-based category, we evaluated both brain and population level approaches. For brain graph classification, we included GAT (Veličković et al., 2017), BrainGNN (Li et al., 2019), and TSEN (Hu et al., 2023), which operate on individual functional connectivity graphs and aim to predict individual-specific diagnostic labels. In comparison, population graph models such as Population-GCN (Parisot et al., 2018), EV-GCN (Huang and Chung, 2020), and LG-GNN (Zhang et al., 2023a) integrate non-imaging variables and are trained in a transductive setting.

Our proposed methods include ANR-GAT, which enhances brain network representation learning through attention graph network and node reassignment strategies, and B2P-GL, which integrates individual brain features with condition-based population modeling and multimodal phenotypic fusion.

As shown in Table 3, our proposed models outperform existing baselines across most datasets and evaluation metrics. Among non-graph models, BrainNetCNN and BrainNetTransformer exhibit solid results, particularly on ADHD-200 dataset. However, their inability to explicitly model relational structure between brain regions or individuals limits their generalizability.

Among individual-level graph models, ANR-GAT achieves the best accuracy on ABIDE I and ADHD-200. On ABIDE I, it improves accuracy and AUC by 3.6% and 3.7% over the previous best (TSEN), and also yields gains in both specificity and sensitivity. On ADHD-200, it raises AUC by 3.1% and sensitivity by 4.0%, showing stronger detection of neurodevelopmental patterns. Although its performance on REST-meta-MDD is slightly below TSEN, it is more stable with lower variance.

At the population level, B2P-GL achieves top or second-best results on all datasets. On ABIDE I, it improves accuracy by 3.3% and specificity by 7.3% over LG-GNN. On ADHD-200, the model improves accuracy by 12.7% and sensitivity by 6.9% over LG-GNN. On REST-meta-MDD, it improves accuracy by 2.1% and achieves the highest sensitivity, exceeding LG-GNN by 13.4%.

These results highlight the effectiveness of our two-stage strategy, which first refines individual brain representations and then leverages condition-based population modeling. By jointly incorporating functional connectivity and phenotypic features, our models capture individual variability while remaining robust across disorders with distinct neurobiological signatures.

#### 5.4. Analysis of Brain Representative Learning

The semantic similarity used for edge construction and the adaptive node reassignment mechanism are two key components in the brain representation learning stage. In this section, we perform targeted evaluations of both modules to assess their individual contributions and effectiveness in improving the performance of brain graph representations.

##### 5.4.1. Effectiveness of Semantic Similarity in Edge

To evaluate the effectiveness of brain region similarity as an edge definition compared to traditional approaches in brain networks, we conducted a comprehensive analysis using the following edge definitions for the brain graph representation learning: (1) Pearson Correlation with global regression (GR), (2) Pearson Correlation without global regression (NGR), (3) Partial Correlation with GR, (4) Transfer Entropy with GR, and (5) Semantic Similarity of brain regions. Here, global regression refers to the removal of the global mean time series from all brain region signals before computing Pearson or partial correlations.

The results in Table 4 indicate that using semantic similarity for edge definition leads to the best overall performance. Compared to the widely used Pearson correlation with global regression, it yields a 0.7% increase in both accuracy and AUC.

This performance gain suggests that semantic similarity enriches the informational content of the brain graph representation by embedding prior anatomical and functional knowledge into the graph structure. Unlike conventional approaches that rely on signal-based correlations, the semantic approach introduces structurally meaningful connections that are less sensitive to noise and inter-individual variability. Overall, the results highlight the value of incorporating language-informed brain priors to complement and enhance traditional neuroimaging-derived connectivity measures.

Table 4: Performance comparison of different edge definitions used in brain graph construction.

| Edge Type                  | ACC (% , $\uparrow$ )            | AUC (% , $\uparrow$ )            | SEN (% , $\uparrow$ )            | SPE (% , $\uparrow$ )            |
|----------------------------|----------------------------------|----------------------------------|----------------------------------|----------------------------------|
| Pearson Correlation (GR)   | 73.0 $\pm$ 0.7                   | 72.5 $\pm$ 0.7                   | 80.1 $\pm$ 2.6                   | 64.9 $\pm$ 2.5                   |
| Pearson Correlation (NGR)  | 72.6 $\pm$ 0.5                   | 71.6 $\pm$ 0.5                   | <b>86.2 <math>\pm</math> 1.7</b> | 56.9 $\pm$ 1.6                   |
| Partial Correlation (GR)   | 72.4 $\pm$ 0.6                   | 72.1 $\pm$ 0.7                   | 77.0 $\pm$ 0.9                   | <b>67.2 <math>\pm</math> 1.9</b> |
| Transfer Entropy (GR)      | 73.0 $\pm$ 1.0                   | 72.5 $\pm$ 1.1                   | 79.5 $\pm$ 1.7                   | 65.5 $\pm$ 3.6                   |
| <b>Semantic Similarity</b> | <b>73.7 <math>\pm</math> 0.6</b> | <b>73.2 <math>\pm</math> 0.6</b> | 80.5 $\pm$ 1.8                   | 65.9 $\pm$ 2.1                   |

In addition, we further evaluated two strategies for computing semantic similarity: (1) lexical embeddings of region names and (2) contextualized embeddings incorporating their concepts. Subsequently, we compared BERT-base (Devlin et al., 2018), a pre-trained language model designed for general tasks, and BioBERT, a biomedical domain-adapted variant. As shown in Table 5, incorporating contextualized concepts led to consistent performance gains. For BERT-base, concept-based embeddings improved accuracy by 0.6%. BioBERT also benefited from concept augmentation, with a 0.4% increase. When comparing models under the same input setting (i.e., concepts), BioBERT outperformed BERT-base by 0.3% in accuracy and 0.4% in AUC, indicating its advantage as a more suitable choice for neurological applications. These results highlight the importance of both domain-adapted language models and concept-level augmentation for capturing meaningful semantic similarity between brain regions.

Table 5: Comparison of brain region similarity strategies using BERT and BioBERT embeddings. “Names” uses lexical embeddings of region names, while “Concepts” incorporates additional anatomical and functional context.

| Scope    | Model   | ACC (% , $\uparrow$ )            | AUC (% , $\uparrow$ )            | SPE (% , $\uparrow$ )            | SEN (% , $\uparrow$ )            |
|----------|---------|----------------------------------|----------------------------------|----------------------------------|----------------------------------|
| Names    | BERT    | 72.8 $\pm$ 0.6                   | 72.3 $\pm$ 0.6                   | 80.2 $\pm$ 1.8                   | 64.4 $\pm$ 2.4                   |
|          | BioBERT | 73.3 $\pm$ 0.8                   | 72.9 $\pm$ 0.8                   | 79.2 $\pm$ 1.5                   | <b>66.5 <math>\pm</math> 1.6</b> |
| Concepts | BERT    | 73.4 $\pm$ 0.5                   | 72.8 $\pm$ 0.6                   | <b>81.7 <math>\pm</math> 2.0</b> | 64.0 $\pm$ 2.5                   |
|          | BioBERT | <b>73.7 <math>\pm</math> 0.6</b> | <b>73.2 <math>\pm</math> 0.6</b> | 80.5 $\pm$ 1.8                   | 65.9 $\pm$ 2.1                   |

#### 5.4.2. Effectiveness of Node Reassignment and Group Size Sensitivity

When training the brain graphs, our adaptive node reassignment module dynamically refines brain region assignments based on input data, enabling a more flexible and personalized representation of functional brain networks. To assess its effectiveness, we performed an ablation study comparing three configurations: (i) ANR-GAT without the node reassignment

module, (ii) a variant where the reassignment mechanism is replaced with a WGAT layer, and (iii) the full proposed ANR-GAT model.

As shown in Table 6, removing the node reassignment module leads to a noticeable drop in model performance, with accuracy and AUC decreasing to 70.6% and 70.4%, respectively. Replacing the adaptive reassignment mechanism with a WGAT layer yields some improvement over the removal case, indicating that incorporating structural grouping is beneficial. However, this variant still falls short of the full ANR-GAT model, which achieves the highest accuracy of 73.7% and AUC of 73.2%. These results demonstrate that our adaptive node reassignment strategy plays a critical role in enabling the model to learn more flexible and individualized brain region groupings, thereby enhancing the robustness and predictive power of the brain graphs.

Table 6: Ablation study of the node reassignment module in ANR-GAT. Top: complete removal. Middle: replacement with a WGAT layer. Bottom: our full proposed model.

| Model Variant         | ACC (% , $\uparrow$ )            | AUC (% , $\uparrow$ )            | SEP (% , $\uparrow$ )            | SEN (% , $\uparrow$ )            |
|-----------------------|----------------------------------|----------------------------------|----------------------------------|----------------------------------|
| w/o Node Reassignment | 70.6 $\pm$ 0.5                   | 70.4 $\pm$ 0.4                   | 72.2 $\pm$ 4.0                   | 68.7 $\pm$ 3.9                   |
| WGAT Replacement      | 72.1 $\pm$ 0.1                   | 71.2 $\pm$ 0.1                   | 84.0 $\pm$ 2.2                   | 58.4 $\pm$ 2.3                   |
| Full ANR-GAT          | <b>73.7 <math>\pm</math> 0.6</b> | <b>73.2 <math>\pm</math> 0.6</b> | <b>80.6 <math>\pm</math> 1.8</b> | <b>65.9 <math>\pm</math> 2.1</b> |

To further examine the sensitivity of our model to the projection space configuration, we evaluated the impact of varying the predefined group size in the feature-to-group mapping component on the ABIDE dataset. The group size determines the granularity of the reassignment space, influencing the capacity of the model to represent diverse node features. Larger group sizes can capture fine-grained clusters but may introduce redundancy, whereas smaller sizes might oversimplify the structural patterns. Our method addresses this trade-off by leveraging a hard assignment mechanism that treats the group size as an upper bound rather than a strict constraint. Groups are dynamically selected based on the data distribution, and only a subset of them is utilized depending on relevance. Empty groups naturally emerge from this process as part of adaptive sparsity, whereby the model prunes uninformative groups. This not only improves computational efficiency but also mitigates overfit. To quantify this behavior, we define the *group assignment ratio* as the proportion of non-empty groups.

As illustrated in Figure 5, the model achieves optimal performance when the group size lies between 60 and 100, given the original node size of 110. Within this range, the model effectively balances expressivity and generalization, capturing discriminative group-level patterns while preserving individual region characteristics. Beyond this interval, although the predefined group size may exceed the original node count, the number of actively used groups grows only marginally. This observation suggests a saturation regime, in which expanding the group size no longer enhances the model’s representational capacity or contributes meaningfully to the encoding of structural information.

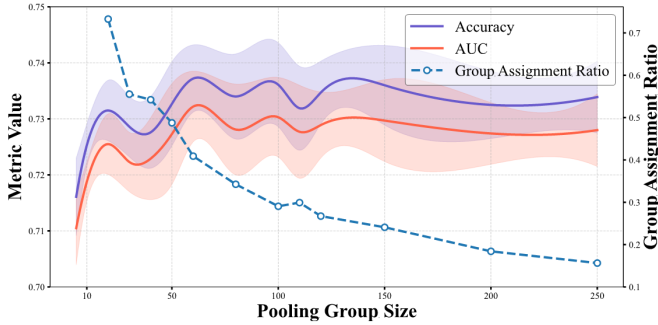


Figure 5: Performance trends in ACC and AUC alongside the group assignment ratio across varying group sizes. The left y-axis shows metric values for ACC and AUC, while the right y-axis represents the group assignment ratio. The results demonstrate the influence of group size on model performance and the actual group assignment numbers using hard assignment.

### 5.5. Analysis of Population Disease Diagnosis

The condition-based population graph construction and the integration of phenotypic information represent two essential components of the population-level disease diagnosis stage. In this section, we evaluate the contribution of phenotypic variables to both the construction of the population graph and the enhancement of individual node features through feature fusion.

#### 5.5.1. Impact of Cross-Condition Population Graph

We evaluated the impact of site, age, and gender conditions on edge generation in the population network. Edge selection dynamically adjusted the top- $k$  edges for each condition, ensuring a proportional total edge count. As shown in Table 7, individual conditions produced comparable results, with gender achieving slightly higher accuracy. Pairwise combinations improved performance incrementally, while integrating all three conditions yielded the best results, with a 1.6% increase in accuracy and a 1.5% increase in AUC. These results demonstrate the importance of leveraging multiple conditions for robust edge generation in brain disorder analysis.

Table 7: Performance comparison using different combinations of site, age, and gender conditions for edge construction.

| Site | Age | Gender | ACC (% , $\uparrow$ )            | AUC (% , $\uparrow$ )            | SPE (% , $\uparrow$ )            | SEN (% , $\uparrow$ )            |
|------|-----|--------|----------------------------------|----------------------------------|----------------------------------|----------------------------------|
| ✓    |     |        | 82.1 $\pm$ 0.4                   | 81.8 $\pm$ 0.5                   | 86.9 $\pm$ 0.7                   | 76.7 $\pm$ 1.6                   |
|      | ✓   |        | 82.1 $\pm$ 0.3                   | 81.8 $\pm$ 0.4                   | 86.3 $\pm$ 0.1                   | 77.3 $\pm$ 0.8                   |
|      |     | ✓      | 82.5 $\pm$ 0.1                   | 82.1 $\pm$ 0.2                   | 87.7 $\pm$ 0.6                   | 76.6 $\pm$ 1.0                   |
| ✓    | ✓   |        | 82.8 $\pm$ 0.9                   | 82.4 $\pm$ 1.0                   | 87.6 $\pm$ 0.3                   | 77.3 $\pm$ 1.8                   |
| ✓    |     | ✓      | 82.7 $\pm$ 0.5                   | 82.5 $\pm$ 0.6                   | 86.0 $\pm$ 0.9                   | <b>79.0 <math>\pm</math> 1.8</b> |
|      | ✓   | ✓      | 82.6 $\pm$ 0.5                   | 82.3 $\pm$ 0.5                   | 86.2 $\pm$ 1.3                   | 78.4 $\pm$ 0.4                   |
| ✓    | ✓   | ✓      | <b>83.4 <math>\pm</math> 0.5</b> | <b>83.0 <math>\pm</math> 0.3</b> | <b>88.9 <math>\pm</math> 0.5</b> | 77.1 $\pm$ 0.1                   |

To investigate the impact of condition-based graph construction and the corresponding heterogeneous modeling strategy, we compared three edge generation and graph learning methods.

Firstly, we constructed a phenotypic-brain similarity graph, in which edges are based on pure similarity of phenotypic and brain features, without differentiating between specific demographic categories. Since no condition type is encoded in the

graph structure, we apply a standard GCN that treats all edges uniformly. This serves as our baseline, where neither edge generation nor model training is aware of demographic distinctions.

We then evaluated the condition-based population graph, where edges are constructed based on shared categorical attributes. To assess the benefit of allowing information exchange across demographic boundaries, we compared two variants: same-category edges, which connect the same category in one condition, and cross-category edges, which also allow links across different categories. The HGCN was employed to effectively model the multiple condition-specific edge types by assigning distinct transformation functions to each relation.

As shown in Table 8, the GCN trained on the phenotypic-brain similarity graph achieves moderate performance. In contrast, our HGCN applied to the same condition-based graph yields clear performance gains. Notably, when cross-category edges are included, allowing information to flow across demographic boundaries, our model achieves the best results, with a 1.4% improvement in accuracy and 1.3% in AUC over the baseline. These experiments highlight the advantage of leveraging inter-demographic relations for more effective population-level graph learning.

Table 8: Performance comparison of different edge construction strategies and model architectures. The Phenotypic-Brain Similarity graph uses a standard GCN without condition-based modeling.

| Edge Type / Model                          | ACC(% , $\uparrow$ )             | AUC(% , $\uparrow$ )             | SPE (% , $\uparrow$ )            | SEN (% , $\uparrow$ ) |
|--|----------------------------------|----------------------------------|----------------------------------|-----------------------|
| Phenotypic-Brain Similarity (GCN)          | 82.0 $\pm$ 0.5                   | 81.7 $\pm$ 0.5                   | 85.3 $\pm$ 1.9                   | 78.1 $\pm$ 1.9        |
| Condition-based: Same-category (HGCN)      | 82.0 $\pm$ 0.5                   | 81.7 $\pm$ 0.6                   | 86.6 $\pm$ 0.7                   | 76.8 $\pm$ 1.5        |
| Condition-based: Different-category (HGCN) | <b>83.4 <math>\pm</math> 0.4</b> | <b>83.0 <math>\pm</math> 0.3</b> | <b>88.9 <math>\pm</math> 0.5</b> | 77.1 $\pm$ 0.1        |

#### 5.5.2. Impact of Phenotypic Feature Fusion

To assess the contribution of phenotypic information to ASD classification, we investigated how fusing individual-level attributes with brain representations influences model performance on the ABIDE I dataset. The phenotypic features considered in this analysis include site, age, gender, and IQ.

As shown in Table 9, integrating individual features leads to varying degrees of performance improvement. Among all features, IQ yields the most notable gain, substantially enhancing classification accuracy and AUC. Combining multiple features results in further improvements: both pairwise and triplet combinations outperform single-feature fusion, indicating that these attributes provide complementary information. The best performance is achieved when all four features are fused, leading to a 6.3% increase in accuracy and a 6.1% gain in AUC compared to using IQ alone. These findings highlight the value of incorporating diverse phenotypic sources. By capturing individual differences beyond imaging data, the model benefits from a more holistic individual representation, ultimately improving its ability to detect disorder-related patterns.

To evaluate the effectiveness of integrating phenotypic features, we conduct a series of fusion experiments using various strategies. Specifically, we compare four approaches: (i) add

Table 9: Impact of different phenotypic feature combinations on performance when fused with brain representations. The first row shows results without phenotypic fusion.

| Site | Age | Gender | IQ | ACC(%, $\uparrow$ )              | AUC(%, $\uparrow$ )              | SPE(%, $\uparrow$ )              | SEN(%, $\uparrow$ )              |
|------|-----|--------|----|----------------------------------|----------------------------------|----------------------------------|----------------------------------|
|      |     |        |    | 77.1 $\pm$ 0.4                   | 76.7 $\pm$ 0.4                   | 82.1 $\pm$ 1.4                   | 71.3 $\pm$ 1.1                   |
| ✓    |     |        |    | 77.3 $\pm$ 0.4                   | 77.1 $\pm$ 0.5                   | 80.1 $\pm$ 0.7                   | 74.2 $\pm$ 1.2                   |
| ✓    | ✓   |        |    | 77.6 $\pm$ 0.9                   | 77.3 $\pm$ 0.9                   | 82.3 $\pm$ 0.9                   | 72.2 $\pm$ 1.1                   |
| ✓    |     | ✓      |    | 77.3 $\pm$ 0.7                   | 77.0 $\pm$ 0.8                   | 81.2 $\pm$ 0.8                   | 72.8 $\pm$ 2.0                   |
| ✓    |     |        | ✓  | 82.1 $\pm$ 0.6                   | 81.9 $\pm$ 0.6                   | 84.8 $\pm$ 0.9                   | <b>79.1 <math>\pm</math> 1.0</b> |
| ✓    | ✓   | ✓      |    | 77.8 $\pm$ 0.5                   | 77.9 $\pm$ 0.6                   | 81.5 $\pm$ 2.0                   | 74.4 $\pm$ 1.2                   |
| ✓    | ✓   | ✓      | ✓  | <b>83.4 <math>\pm</math> 0.5</b> | <b>83.0 <math>\pm</math> 0.3</b> | <b>88.9 <math>\pm</math> 0.5</b> | 77.1 $\pm$ 0.1                   |

fusion, which combines features through element-wise addition; (ii) concat fusion, which concatenates feature vectors before transformation; (iii) attention fusion, which assigns adaptive weights to different modalities using a learned attention mechanism; and (iv) gated fusion (ours), which employs a gating module to selectively control the contribution of each feature dimension.

As shown in Table 10, all fusion-based methods improve performance compared to the baseline without phenotypic fusion, confirming the benefit of incorporating individual-level information. Notably, the gated fusion approach achieves the highest overall accuracy, with a 6.3% improvement over the non-fusion baseline. It also yields marked gains in AUC and specificity, suggesting enhanced discriminative ability and reduced false positives. Compared to standard fusion strategies, the gated mechanism offers consistent and meaningful improvements across all evaluation metrics.

These results demonstrate that gating provides a more effective and flexible means of integrating heterogeneous phenotypic features. By dynamically adjusting the contribution of each input, the model is better equipped to capture individual-specific variations relevant to the classification task.

Table 10: Performance of various phenotype feature fusion methods, including attention-based, additive, and gated fusion approaches.

| Approach            | ACC(%, $\uparrow$ )              | AUC(%, $\uparrow$ )              | SEP(%, $\uparrow$ )              | SEN(%, $\uparrow$ )              |
|---------------------|----------------------------------|----------------------------------|----------------------------------|----------------------------------|
| No Feature Fusion   | 77.1 $\pm$ 0.4                   | 76.7 $\pm$ 0.4                   | 82.1 $\pm$ 1.4                   | 71.3 $\pm$ 1.1                   |
| Attention Fusion    | 82.8 $\pm$ 0.6                   | 82.5 $\pm$ 0.6                   | 86.3 $\pm$ 1.7                   | 78.7 $\pm$ 1.7                   |
| Add Fusion          | 82.5 $\pm$ 0.7                   | 82.2 $\pm$ 0.8                   | 86.3 $\pm$ 0.5                   | 78.2 $\pm$ 1.4                   |
| Concat Fusion       | 83.0 $\pm$ 0.7                   | 82.7 $\pm$ 0.7                   | 87.3 $\pm$ 1.5                   | 78.1 $\pm$ 1.4                   |
| Gated Fusion (Ours) | <b>83.4 <math>\pm</math> 0.4</b> | <b>83.0 <math>\pm</math> 0.3</b> | <b>88.9 <math>\pm</math> 0.5</b> | <b>77.1 <math>\pm</math> 0.1</b> |

## 5.6. Analysis of Loss Function in Two Stage

To investigate the impact of incorporating similarity loss in different training stages, we compare the performance of the model with and without this loss in both Stage 1 and Stage 2. The similarity loss is designed to enforce consistency in feature representations between similar instances, potentially enhancing the discriminative power of learned embeddings.

Table 11 summarizes the classification performance under four configurations: with and without similarity loss in Stage 1, and with and without similarity loss in Stage 2. As shown in the table, adding similarity loss in Stage 1 leads to only a marginal improvement in accuracy. This suggests that the similarity loss alone has a limited impact when used in the early

stage of feature learning, where features are still coarse and less structured. In contrast, the addition of similarity loss in Stage 2, where graph construction is based on feature similarity, results in a more significant performance gain. Specifically, Stage 2 with similarity loss improves accuracy and AUC by 1.4% compared to its counterpart without similarity loss. This indicates that the similarity constraint becomes more effective when the model already leverages similarity-based structures, reinforcing the consistency of neighboring nodes in the population-level graph. Overall, these findings demonstrate that the benefit of similarity loss is more pronounced in the second stage, where feature similarity directly contributes to the graph structure and phenotypic fusion.

Table 11: Performance comparison under four training configurations: with or without similarity loss in Stage 1 and Stage 2.

| Configuration          | ACC(%, $\uparrow$ )              | AUC(%, $\uparrow$ )              | SPE(%, $\uparrow$ )              | SEN(%, $\uparrow$ )              |
|------------------------|----------------------------------|----------------------------------|----------------------------------|----------------------------------|
| Stage 1 w/o similarity | 73.4 $\pm$ 0.9                   | 72.8 $\pm$ 1.0                   | 81.3 $\pm$ 1.6                   | 64.3 $\pm$ 2.8                   |
| Stage 1 w/ similarity  | 73.7 $\pm$ 0.6                   | 73.2 $\pm$ 0.6                   | 80.6 $\pm$ 1.8                   | 65.9 $\pm$ 2.1                   |
| Stage 2 w/o similarity | 82.0 $\pm$ 0.6                   | 81.6 $\pm$ 0.6                   | 86.6 $\pm$ 1.2                   | 76.6 $\pm$ 1.5                   |
| Stage 2 w/ similarity  | <b>83.4 <math>\pm</math> 0.4</b> | <b>83.0 <math>\pm</math> 0.3</b> | <b>88.9 <math>\pm</math> 0.5</b> | <b>77.1 <math>\pm</math> 0.1</b> |

## 5.7. Interpretive Analysis

In this subsection, we analyzed the interpretability of our proposed model in identifying critical nodes and node reassignment groups for brain graphs.

### 5.7.1. Node Importance

To identify the brain regions most indicative of each disorder, we applied Grad-CAM (Selvaraju et al., 2017) to compute the gradient of the model’s output with respect to node features after the first GAT layer. The top-10 most influential nodes for ASD, ADHD, and MDD are visualized in Figure 6, with detailed region names listed in Table 12. These regions were further analyzed to interpret the disorder-specific and shared neurobiological patterns learned by the model.

For the two neurodevelopmental disorders, ASD and ADHD, the most predictive brain regions are predominantly located within the limbic and basal ganglia networks. Among these, the nucleus accumbens (Accbns.R, Accbns.L), a key region involved in reward processing and motivation, was consistently identified across both models. This structure has been implicated in social motivation deficits in ASD and in impulsive decision-making in ADHD (Dichter et al., 2012; Dias et al., 2013). Similarly, the caudate nucleus (Caud.R, Caud.L), which plays a critical role in motor control and executive functioning, also emerged as a key region. Prior studies have reported aberrant activation patterns of the caudate in both ASD and ADHD (O’Dwyer et al., 2016), aligning with our findings. The frontal pole (FP.R), part of the default mode network (DMN), was also identified as a shared high-impact region across both disorders. This region is involved in higher-order cognitive and affective regulation and is frequently altered in neurodevelopmental conditions (Hrvoj-Mihic and Semendeferi, 2019). In

Table 12: Top-10 most predictive brain regions in ASD, ADHD, and MDD classification models.

| Functional Network     | ASD Regions  | ADHD Regions   | MDD Regions  |
|------------------------|--|--|--|
| Frontoparietal Network | –  | –  | Left Middle Frontal Gyrus (MFG.L), Right Inferior Frontal Triangular (IFGtriang.R), Left Inferior Frontal Triangular (IFGtriang.L), Left Middle Orbital Gyrus (ORBmid.L) |
| Default Mode Network   | Right Frontal Pole (FPR)   | Right Frontal Pole (FPR)   | Right Angular Gyrus (ANG.R), Left Angular Gyrus (ANG.L), Right Precuneus (PCUN.R)  |
| Limbic Network         | Right Planum Polare (PP.R), Left Planum Polare (PP.L), Right Accumbens (Accbns.R), Left Accumbens (Accbns.L) | Right Subcallosal Cortex (SC.R), Right Accumbens (Accbns.R), Left Accumbens (Accbns.L)                                 | Right Superior Orbital Gyrus (ORBsup.R)  |
| Visual Network         | Right Occipital Pole (OP.R)  | Right Occipital Pole (OP.R)  | Right Superior Occipital Gyrus (SOG.R)   |
| Basal Ganglia Network  | Right Caudate (Caud.R), Left Pallidum (Pall.L), Right Pallidum (Pall.R), Left Putamen (Put.L)                | Right Caudate (Caud.R), Left Caudate (Caud.L), Left Pallidum (Pall.L), Right Thalamus (Thal.R), Left Thalamus (Thal.L) | –  |
| Sensorimotor Network   | –  | –  | Right Precentral Gyrus (PreCG.R)   |

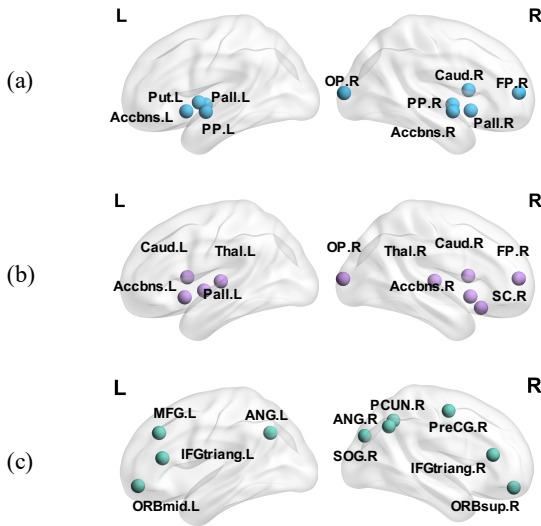


Figure 6: Visualization of the top-10 most frequently identified brain region pairs across disorders, shown in both right and left hemisphere views. (a) In the ASD model, the most important regions are located within the limbic and basal ganglia networks. (b) In the ADHD model, key regions are similarly concentrated in the limbic and basal ganglia networks. (c) In the MDD model, the most influential regions are primarily distributed within the frontoparietal and default mode networks.

addition, the occipital pole (OP.R), belonging to the visual network, was identified as important in both ASD and ADHD, reflecting known abnormalities in visual processing (Jung et al., 2019; Wu et al., 2020).

Despite these commonalities, several disorder-specific patterns were observed. In ASD, the planum polare (PP.R, PP.L), a region involved in auditory and language processing, was ranked highly. This finding is consistent with prior reports of atypical auditory function in individuals with autism (Abrams et al., 2019). In contrast, the thalamus (Thal.R, Thal.L) was more prominent in the ADHD model. As a central hub for relaying sensory and motor signals, thalamic dysfunction has been associated with attentional deficits and treatment responsiveness in ADHD (Bailey and Joyce, 2015). These findings suggest that while ASD and ADHD share alterations in core

subcortical circuits, each disorder also involves distinct functional substrates.

In comparison, the most discriminative brain regions for MDD were primarily located within the frontoparietal network (FPN) and the default mode network (DMN), two canonical resting-state networks consistently implicated in mood disorders. The FPN is involved in high-level cognitive functions, including working memory and cognitive control, while the DMN supports self-referential thought and affective processing (Belleau et al., 2023). Dysregulation within and between these networks has been widely reported in MDD and is thought to contribute to core symptoms such as rumination and cognitive inflexibility (Marchetti et al., 2012).

In summary, our model identifies both shared and disorder-specific neurofunctional signatures. ASD and ADHD show substantial overlap, particularly in the limbic and basal ganglia networks, while MDD is primarily associated with disruptions in large-scale cognitive and affective systems. These findings underscore both convergent and divergent neurobiological pathways across diagnostic categories and suggest potential network-level targets for biomarker discovery and interventions.

### 5.7.2. Group Reassignment

To identify interpretable groupings, we calculated the probability of each node pair being assigned to the same group across samples and selected the top 10 pairs with the highest co-assignment frequency. These frequently co-assigned pairs are visualized in Figure 7. To further examine the underlying structure, we organized these pairs into connected components, which reflect clusters of brain regions with similar feature representations and a high likelihood of joint assignment. The details of these components are provided in Table 13.

The ASD model revealed frequent co-assignment of regions spanning the basal ganglia, limbic, visual, and default mode networks. Notably, subcortical structures such as the pallidum (Pall.L, Pall.R), thalamus (Thal.R), and hippocampus (Hip.L, Hip.R) emerged as highly connected, indicating disruptions in motor coordination, memory, and socio-emotional processing (Pessoa, 2017). The ADHD model showed a dominant group

Table 13: Top-10 high-frequency node pair groups across ASD, ADHD, and MDD models.

| Disorder | Group | Functional Network        | Brain Regions   |
|----------|-------|---------------------------|---|
| ASD      | 1     | Visual Network            | Right Intracalcarine Cortex (Calc.R), Left Intracalcarine Cortex (Calc.L), Right Supracalcarine Cortex (SCLC.R)   |
|          | 2     | Basal Ganglia Network     | Right Thalamus (Thal.R), Right Pallidum (Pall.R)  |
|          |       | Limbic Network            | Left Hippocampus (Hip.L), Right Hippocampus (Hip.R)   |
|          |       | Default Mode Network      | Left Parahippocampal Gyrus (PHG.L), Right Parahippocampal Gyrus (PHG.R)   |
| ADHD     | 1     | Visual Network            | Right Intracalcarine Cortex (Calc.R), Left Intracalcarine Cortex (Calc.L), Right Lingual Gyrus (Ling.R), Left Lingual Gyrus (Ling.L), Right Cuneal Cortex (Cun.R), Left Cuneal Cortex (Cun.L), Right Supracalcarine Cortex (SCLC.R) |
| MDD      | 1     | Sensorimotor Network      | Left Rolandic Operculum (ROL.L), Right Rolandic Operculum (ROL.R), Left Heschl Gyrus (HES.L), Right Heschl Gyrus (HES.R), Left Superior Temporal Gyrus (STG.L)  |
|          |       | Ventral Attention Network | Left Insula (INS.L), Right Insula (INS.R)   |
|          | 2     | Visual Network            | Left Calcarine Cortex (CAL.L), Right Calcarine Cortex (CAL.R), Left Lingual Gyrus (LING.L), Right Lingual Gyrus (LING.R)  |

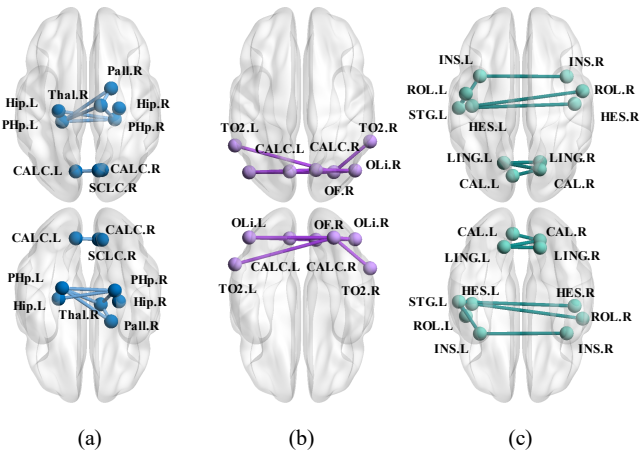


Figure 7: Brain region connections based on the top-10 highest-frequency node pairs, visualized in dorsal and ventral view. (a) The ASD model demonstrates reassigned connections primarily located in subcortical regions. (b) The ADHD model shows reassignments concentrated in the occipital lobe. (c) The MDD model exhibits grouping in prefrontal regions.

localized within the visual network. Frequently co-assigned regions included the bilateral intracalcarine cortex (Calc.L, Calc.R), lingual gyrus (Ling.L, Ling.R), cuneal cortex (Cun.L, Cun.R), and supracalcarine cortex (SCLC.R). These anatomically adjacent occipital regions are functionally linked to early-stage visual processing (Gage and Baars, 2018). For MDD, the principal grouping encompassed regions from the sensorimotor and ventral attention networks. Frequently co-assigned areas included the Rolandic operculum (ROL.L, ROL.R), Heschl’s gyrus (HES.L, HES.R), superior temporal gyrus (STG.L), and bilateral insula (INS.L, INS.R), forming an integrated network that mediates sensorimotor processing, auditory integration, and affective salience detection (Dziedzic et al., 2022; Have, 2007).

These region groupings emerged from the model’s learned co-assignment patterns, suggesting that they may share similar feature representations or jointly aid in distinguishing brain disorders.

## 6. Discussion and Conclusion

In this study, we proposed a B2P-GL framework to enhance brain network representation and reduce individual bias in brain disorder analysis using medical imaging. In the first stage, termed brain representation learning, we leveraged the knowledge embedded in brain atlases, refining the graph through node reassignment to improve brain representation. In the second stage, termed population disorder diagnosis, we incorporated personal characteristics to estimate confounding effects and fused these with brain features. Our framework outperformed various GNNs in FC-based disorder identification and provided clinical interpretability, demonstrating significant potential for application in the analysis of diverse neurodevelopmental disorders.

Overall, our work demonstrates a notable level of superiority. (1) Experiments on three publicly available brain disorder datasets show that our framework consistently outperforms existing GNN-based methods in functional connectivity-based classification, confirming its robustness and broad applicability. (2) Ablation studies further highlight the critical roles of our key design components, including semantic brain graph refinement and node reassignment in the first stage, which enhance the expressiveness of brain representations, as well as condition-based population modeling for confound mitigation and gated fusion for integrating multi-modal phenotypic data in the second stage. (3) The interpretive analysis reveals meaningful patterns in brain functional connectivity, offering valuable insights into disorder-specific alterations and enhancing the clinical relevance of the learned representations.

Despite these promising findings, several limitations remain. The brain region embeddings used in our method are derived from general-purpose large language models, which may not fully reflect domain-specific anatomical and functional nuances. Incorporating structured neuroscience knowledge, such as expert-curated ontologies or dedicated anatomical corpora, could yield more robust and biologically grounded representations. Additionally, the variability inherent in large language models introduces uncertainty that requires further control, especially when generalizing across datasets. Future work could explore domain-adaptive fine-tuning strategies and extend the

framework to other imaging modalities or clinical conditions to further validate its utility and versatility.

## Declaration of Competing Interest

The authors declare that they have no known competing financial interests or personal relationships that could have appeared to influence the work reported in this paper.

## Data and code availability

We will share our code at <https://github.com/GuoLab-UESTC> after this manuscript is accepted for publication. All the datasets used in our work are sourced from public datasets.

## Acknowledgments

This work was supported in part by the STI 2030–Major Projects under grant 2022ZD0208500, in part by the National Key Research and Development Program of China under grant 2023YFF1204200, in part by the Sichuan Science and Technology Program under grant 2024NSFTD0032, grant 2024NSFJQ0004 and grant DQ202410, and in part by the Natural Science Foundation of Chongqing, China under grant CSTB2024NSCQ-MSX0627, in part by the Science and Technology Research Program of Chongqing Education Commission of China under Grant KJZD-K202401603, and in part by the China Postdoctoral Science Foundation under grant 2024M763876.

## References

Abrams, D.A., Padmanabhan, A., Chen, T., Odriozola, P., Baker, A.E., Kochalka, J., Phillips, J.M., Menon, V., 2019. Impaired voice processing in reward and salience circuits predicts social communication in children with autism. *elife* 8, e39906.

Achiam, J., Adler, S., Agarwal, S., Ahmad, L., Akkaya, I., Aleman, F.L., Almeida, D., Altenschmidt, J., Altman, S., Anadkat, S., et al., 2023. Gpt-4 technical report. *arXiv preprint arXiv:2303.08774*.

Arbabshirani, M.R., Plis, S., Sui, J., Calhoun, V.D., 2017. Single subject prediction of brain disorders in neuroimaging: Promises and pitfalls. *Neuroimage* 145, 137–165.

Arora, N.K., Nair, M., Gulati, S., Deshmukh, V., Mohapatra, A., Mishra, D., Patel, V., Pandey, R.M., Das, B.C., Divan, G., et al., 2018. Neurodevelopmental disorders in children aged 2–9 years: Population-based burden estimates across five regions in india. *PLoS medicine* 15, e1002615.

Bailey, T., Joyce, A., 2015. The role of the thalamus in adhd symptomatology and treatment. *Applied Neuropsychology: Child* 4, 89–96.

Bannadabhavi, A., Lee, S., Deng, W., Ying, R., Li, X., 2023. Community-aware transformer for autism prediction in fmri connectome, in: International Conference on Medical Image Computing and Computer-Assisted Intervention, Springer. pp. 287–297.

Belleau, E.L., Kremens, R., Bolton, T.A., Bondy, E., Pisoni, A., Auerbach, R.P., Pizzagalli, D.A., 2023. Default mode and frontoparietal network dynamics: Associations with familial risk for depression and stress sensitivity. *Journal of mood and anxiety disorders* 1, 100001.

Bellec, P., et al., 2017. The neuro bureau adhd-200 preprocessed repository. *NeuroImage* 144, 275–286.

Brown, M.R., Sidhu, G.S., Greiner, R., Asgarian, N., Bastani, M., Silverstone, P.H., Greenshaw, A.J., Dursun, S.M., 2012. Adhd-200 global competition: diagnosing adhd using personal characteristic data can outperform resting state fmri measurements. *Frontiers in systems neuroscience* 6, 69.

Bzdok, D., Thieme, A., Levkovskyy, O., Wren, P., Ray, T., Reddy, S., 2024. Data science opportunities of large language models for neuroscience and biomedicine. *Neuron* 112, 698–717.

Campbell, A., Zippo, A.G., Passamonti, L., Toschi, N., Lio, P., 2023. Dyndepnet: Learning time-varying dependency structures from fMRI data via dynamic graph structure learning, in: ICML 3rd Workshop on Interpretable Machine Learning in Healthcare (IMLH). URL: <https://openreview.net/forum?id=CyfKnG8nXr>.

Cao, M., Yang, M., Qin, C., Zhu, X., Chen, Y., Wang, J., Liu, T., 2021. Using deepgen to identify the autism spectrum disorder from multi-site resting-state data. *Biomedical Signal Processing and Control* 70, 103015.

Chen, A., Rossi, R.A., Park, N., Trivedi, P., Wang, Y., Yu, T., Kim, S., Dernoncourt, F., Ahmed, N.K., 2024a. Fairness-aware graph neural networks: A survey. *ACM Transactions on Knowledge Discovery from Data* 18, 1–23.

Chen, W., Yang, J., Sun, Z., Zhang, X., Tao, G., Ding, Y., Gu, J., Bu, J., Wang, H., 2024b. Deepasd: a deep adversarial-regularized graph learning method for asd diagnosis with multimodal data. *Translational Psychiatry* 14, 375.

Chen, X., Lu, B., Li, H.X., Li, X.Y., Wang, Y.W., Castellanos, F.X., Cao, L.P., Chen, N.X., Chen, W., Cheng, Y.Q., et al., 2022a. The direct consortium and the rest-meta-mdd project: towards neuroimaging biomarkers of major depressive disorder. *Psychoradiology* 2, 32–42.

Chen, Y., Yan, J., Jiang, M., Zhang, T., Zhao, Z., Zhao, W., Zheng, J., Yao, D., Zhang, R., Kendrick, K.M., et al., 2022b. Adversarial learning based node-edge graph attention networks for autism spectrum disorder identification. *IEEE Transactions on Neural Networks and Learning Systems*.

Cohen, I., Huang, Y., Chen, J., Benesty, J., Benesty, J., Chen, J., Huang, Y., Cohen, I., 2009. Pearson correlation coefficient. *Noise reduction in speech processing*, 1–4.

Craddock, C., Benhajali, Y., Chu, C., Chouinard, F., Evans, A., Jakab, A., Khundrakpam, B.S., Lewis, J.D., Li, Q., Milham, M., Yan, C., Bellec, P., 2013. The neuro bureau preprocessing initiative: open sharing of preprocessed neuroimaging data and derivatives, in: *Neuroinformatics 2013*, Stockholm, Sweden.

Cui, H., Dai, W., Zhu, Y., Kan, X., Gu, A.A.C., Lukemire, J., Zhan, L., He, L., Guo, Y., Yang, C., 2022. Braingb: a benchmark for brain network analysis with graph neural networks. *IEEE transactions on medical imaging* 42, 493–506.

Devlin, J., Chang, M., Lee, K., Toutanova, K., 2018. BERT: pre-training of deep bidirectional transformers for language understanding. *CoRR abs/1810.04805*. URL: <http://arxiv.org/abs/1810.04805>, *arXiv:1810.04805*.

Di Martino, A., et al., 2014. The autism brain imaging data exchange: Towards a large-scale evaluation of the intrinsic brain architecture in autism. *Molecular Psychiatry* 19, 659–667.

Dias, T.G.C., Wilson, V.B., Bathula, D.R., Iyer, S.P., Mills, K.L., Thurlow, B.L., Stevens, C.A., Musser, E.D., Carpenter, S.D., Grayson, D.S., et al., 2013. Reward circuit connectivity relates to delay discounting in children with attention-deficit/hyperactivity disorder. *European Neuropsychopharmacology* 23, 33–45.

Dichter, G.S., Felder, J.N., Green, S.R., Rittenberg, A.M., Sasson, N.J., Bodfish, J.W., 2012. Reward circuitry function in autism spectrum disorders. *Social cognitive and affective neuroscience* 7, 160–172.

Dosovitskiy, A., Beyer, L., Kolesnikov, A., Weissenborn, D., Zhai, X., Unterthiner, T., Dehghani, M., Minderer, M., Heigold, G., Gelly, S., et al., 2020. An image is worth 16x16 words: Transformers for image recognition at scale. *arXiv preprint arXiv:2010.11929*.

Dziedzic, T.A., Bala, A., Marchel, A., 2022. Anatomical aspects of the insula, opercula and peri-insular white matter for a transcortical approach to insular glioma resection. *Neurosurgical Review* 45, 793–806.

Ferrari, E., Bosco, P., Calderoni, S., Oliva, P., Palumbo, L., Spera, G., Fantacci, M.E., Retico, A., 2020. Dealing with confounders and outliers in classification medical studies: The autism spectrum disorders case study. *Artificial Intelligence in Medicine* 108, 101926.

Finlay-Jones, A., Varcin, K.J., Leonard, H., Bosco, A., Alvares, G., Downs, J., 2019. Very early identification and intervention for infants at risk of neurodevelopmental disorders: A transdiagnostic approach. *Child Development Perspectives* doi:10.1111/CDEP.12319.

Gage, N.M., Baars, B.J., 2018. Chapter 2 - the brain, in: Gage, N.M., Baars, B.J. (Eds.), *Fundamentals of Cognitive Neuroscience (Second Edition)*. second edition ed., Academic Press, San Diego, pp. 17–52. doi:<https://doi.org/10.1016/B978-0-12-803813-0.00002-7>.

- Gallo, S., El-Gazzar, A., Zhutovsky, P., Thomas, R.M., Javaheripour, N., Li, M., Bartova, L., Bathula, D., Dannlowski, U., Davey, C., et al., 2023. Functional connectivity signatures of major depressive disorder: machine learning analysis of two multicenter neuroimaging studies. *Molecular Psychiatry* 28, 3013–3022.
- Geerligs, L., Tsvetanov, K.A., Henson, R.N., 2017. Challenges in measuring individual differences in functional connectivity using fmri: the case of healthy aging. *Human brain mapping* 38, 4125–4156.
- Gordon, E.M., Nelson, S.M., 2021. Three types of individual variation in brain networks revealed by single-subject functional connectivity analyses. *Current Opinion in Behavioral Sciences* 40, 79–86.
- Have, M.V.P.C., 2007. Heschl's gyrus, posterior superior temporal gyrus. *J Neurophysiol* 97, 2075–2082.
- Hinshaw, S., 2018. Attention deficit hyperactivity disorder (adhd): Controversy, developmental mechanisms, and multiple levels of analysis. *Annual review of clinical psychology* 14, 291–316. doi:10.1146/annurev-clinpsy-050817-084917.
- Hodges, H., Fealko, C., Soares, N., 2020. Autism spectrum disorder: definition, epidemiology, causes, and clinical evaluation. *Translational Pediatrics* 9, S55 – S65. doi:10.21037/tp.2019.09.09.
- Hrvoy-Mihic, B., Semendeferi, K., 2019. Neurodevelopmental disorders of the prefrontal cortex in an evolutionary context. *Progress in Brain Research* 250, 109–127.
- Hu, J., Huang, Y., Dong, S., 2023. Transformer and snowball graph convolution learning for brain functional network analysis, in: 2023 IEEE International Conference on Bioinformatics and Biomedicine (BIBM), pp. 2809–2816. doi:10.1109/BIBM58861.2023.10385857.
- Huang, J., Wang, M., Ju, H., Shi, Z., Ding, W., Zhang, D., 2023. Sd-cnn: A static-dynamic convolutional neural network for functional brain networks. *Medical Image Analysis* 83, 102679.
- Huang, Y., Chung, A.C., 2020. Edge-variational graph convolutional networks for uncertainty-aware disease prediction, in: International Conference on Medical Image Computing and Computer-Assisted Intervention, Springer. pp. 562–572.
- Huang, Y., Yang, X., Liu, L., Zhou, H., Chang, A., Zhou, X., Chen, R., Yu, J., Chen, J., Chen, C., et al., 2024. Segment anything model for medical images? *Medical Image Analysis* 92, 103061.
- Jain, V., Chadha, A., 2021. Word vectors. Distilled AI <https://aman.ai>.
- Ji, J., Ren, Y., Lei, M., 2022. Fc-hat: hypergraph attention network for functional brain network classification. *Information Sciences* 608, 1301–1316.
- Jiang, H., Cao, P., Xu, M., Yang, J., Zaijane, O., 2020. Hi-gcn: A hierarchical graph convolutional network for graph embedding learning of brain network and brain disorders prediction. *Computers in Biology and Medicine* 127, 104096.
- Jung, M., Tu, Y., Lang, C.A., Ortiz, A., Park, J., Jorgenson, K., Kong, X.J., Kong, J., 2019. Decreased structural connectivity and resting-state brain activity in the lateral occipital cortex is associated with social communication deficits in boys with autism spectrum disorder. *Neuroimage* 190, 205–212.
- Kan, X., Dai, W., Cui, H., Zhang, Z., Guo, Y., Yang, C., 2022. Brain network transformer. *Advances in Neural Information Processing Systems* 35, 25586–25599.
- Kawahara, J., Brown, C.J., Miller, S.P., Booth, B.G., Chau, V., Grunau, R.E., Zwicker, J.G., Hamarneh, G., 2017. Brainnetcn: Convolutional neural networks for brain networks; towards predicting neurodevelopment. *NeuroImage* 146, 1038–1049.
- Krizhevsky, A., Sutskever, I., Hinton, G.E., 2017. Imagenet classification with deep convolutional neural networks. *Communications of the ACM* 60, 84–90.
- Ktena, S.I., Parisot, S., Ferrante, E., Rajchl, M., Lee, M., Glocker, B., Rueckert, D., 2018. Metric learning with spectral graph convolutions on brain connectivity networks. *NeuroImage* 169, 431–442.
- Li, S., Zhang, R., 2024. A novel interactive deep cascade spectral graph convolutional network with multi-relational graphs for disease prediction. *Neural Networks* 175, 106285.
- Li, X., Dvornek, N.C., Zhou, Y., Zhuang, J., Ventola, P., Duncan, J.S., 2019. Graph neural network for interpreting task-fMRI biomarkers , 485–493.
- Logothetis, N.K., 2003. The underpinnings of the bold functional magnetic resonance imaging signal. *Journal of Neuroscience* 23, 3963–3971.
- Logothetis, N.K., Wandell, B.A., 2004. Interpreting the bold signal. *Annu. Rev. Physiol.* 66, 735–769.
- Marchetti, I., Koster, E.H., Sonuga-Barke, E.J., De Raedt, R., 2012. The default mode network and recurrent depression: a neurobiological model of cognitive risk factors. *Neuropsychology review* 22, 229–251.
- Masi, A., DeMayo, M.M., Glozier, N., Guastella, A.J., 2017. An overview of autism spectrum disorder, heterogeneity and treatment options. *Neuroscience bulletin* 33, 183–193.
- Milham, M., et al., 2012. The adhd-200 consortium: A model to advance the translational potential of neuroimaging in clinical neuroscience. *Frontiers in Systems Neuroscience* 62.
- Nori, H., King, N., McKinney, S.M., Carignan, D., Horvitz, E., 2023. Capabilities of gpt-4 on medical challenge problems. *arXiv preprint arXiv:2303.13375*.
- O'Dwyer, L., Tanner, C., Van Dongen, E.V., Greven, C.U., Bralten, J., Zwiers, M.P., Franke, B., Heslenfeld, D., Oosterlaan, J., Hoekstra, P.J., et al., 2016. Decreased left caudate volume is associated with increased severity of autistic-like symptoms in a cohort of adhd patients and their unaffected siblings. *PLoS One* 11, e0165620.
- Pan, J., Lin, H., Dong, Y., Wang, Y., Ji, Y., 2022. Mamf-gcn: Multi-scale adaptive multi-channel fusion deep graph convolutional network for predicting mental disorder. *Computers in biology and medicine* 148, 105823.
- Parisot, S., Ktena, S.I., Ferrante, E., Lee, M., Guerrero, R., Glocker, B., Rueckert, D., 2018. Disease prediction using graph convolutional networks: Application to autism spectrum disorder and alzheimer's disease. *Medical image analysis*.
- Park, H.J., Friston, K., 2013. Structural and functional brain networks: from connections to cognition. *Science* 342, 1238411.
- Peng, L., Cai, S., Wu, Z., Shang, H., Zhu, X., Li, X., 2024. Mmgpl: Multimodal medical data analysis with graph prompt learning. *Medical Image Analysis* , 103225.
- Pessoa, L., 2017. A network model of the emotional brain. *Trends in cognitive sciences* 21, 357–371.
- Qin, K., Lei, D., Pinaya, W.H., Pan, N., Li, W., Zhu, Z., Sweeney, J.A., Mechelli, A., Gong, Q., 2022. Using graph convolutional network to characterize individuals with major depressive disorder across multiple imaging sites. *EBioMedicine* 78.
- Rao, A., Monteiro, J.M., Mourao-Miranda, J., Initiative, A.D., et al., 2017. Predictive modelling using neuroimaging data in the presence of confounds. *NeuroImage* 150, 23–49.
- Roland, P., Zilles, K., 1994. Brain atlases - a new research tool. *Trends in Neurosciences* 17, 458–467. doi:10.1016/0166-2236(94)90131-7.
- Scarselli, F., Gori, M., Tsoi, A.C., Hagenbuchner, M., Monfardini, G., 2008. The graph neural network model. *IEEE transactions on neural networks* 20, 61–80.
- Schlichtkrull, M., Kipf, T.N., Bloem, P., Van Den Berg, R., Titov, I., Welling, M., 2018. Modeling relational data with graph convolutional networks, in: The semantic web: 15th international conference, ESWC 2018, Heraklion, Crete, Greece, June 3–7, 2018, proceedings 15, Springer. pp. 593–607.
- Selvaraju, R.R., Cogswell, M., Das, A., Vedantam, R., Parikh, D., Batra, D., 2017. Grad-cam: Visual explanations from deep networks via gradient-based localization, in: Proceedings of the IEEE International Conference on Computer Vision (ICCV), pp. 618–626.
- Shao, L., Fu, C., Chen, X., 2023. A heterogeneous graph convolutional attention network method for classification of autism spectrum disorder. *BMC bioinformatics* 24, 363.
- Tang, H., Ma, G., Zhang, Y., Ye, K., Guo, L., Liu, G., Huang, Q., Wang, Y., Ajilore, O., Leow, A.D., et al., 2023. A comprehensive survey of complex brain network representation. *Meta-Radiology* , 100046.
- Veličković, P., Cucurull, G., Casanova, A., Romero, A., Lio, P., Bengio, Y., 2017. Graph attention networks. *arXiv preprint arXiv:1710.10903*.
- Wang, P., Zhang, H., He, Z., Peng, Z., Yuan, Y., 2024a. ftspl: Enhancing brain analysis with fmri-text synergistic prompt learning, in: International Conference on Medical Image Computing and Computer-Assisted Intervention, Springer. pp. 564–574.
- Wang, W., Xiao, L., Qu, G., Calhoun, V.D., Wang, Y.P., Sun, X., 2024b. Multiview hyperedge-aware hypergraph embedding learning for multisite, multiatlas fmri based functional connectivity network analysis. *Medical Image Analysis* 94, 103144.
- Wang, X., Fang, Y., Wang, Q., Yap, P.T., Zhu, H., Liu, M., 2025. Self-supervised graph contrastive learning with diffusion augmentation for functional mri analysis and brain disorder detection. *Medical Image Analysis* 101, 103403.
- Wen, G., Cao, P., Liu, L., Hao, M., Liu, S., Zheng, J., Yang, J., Zaijane, O.R.,

- Wang, F., 2024. Heterogeneous graph representation learning framework for resting-state functional connectivity analysis. *IEEE Transactions on Medical Imaging* .
- Wu, Z., Luo, Y., Gao, Y., Han, Y., Wu, K., Li, X., 2020. The role of frontal and occipital cortices in processing sustained visual attention in young adults with attention-deficit/hyperactivity disorder: A functional near-infrared spectroscopy study. *Neuroscience Bulletin* 36, 659–663.
- Yan, A., Wang, Y., Zhong, Y., He, Z., Karypis, P., Wang, Z., Dong, C., Gentili, A., Hsu, C.N., Shang, J., et al., 2023. Robust and interpretable medical image classifiers via concept bottleneck models. *arXiv preprint arXiv:2310.03182* .
- Yan, C.G., Chen, X., Li, L., Castellanos, F.X., Bai, T.J., Bo, Q.J., Cao, J., Chen, G.M., Chen, N.X., Chen, W., et al., 2019. Reduced default mode network functional connectivity in patients with recurrent major depressive disorder. *Proceedings of the National Academy of Sciences* 116, 9078–9083.
- Yang, J., Hu, M., Hu, Y., Zhang, Z., Zhong, J., 2023. Diagnosis of autism spectrum disorder (asd) using recursive feature elimination–graph neural network (rfe–ggn) and phenotypic feature extractor (pfe). *Sensors* 23, 9647.
- Ye, Y., Ji, S., 2021. Sparse graph attention networks. *IEEE Transactions on Knowledge and Data Engineering* 35, 905–916.
- Yin, W., Mostafa, S., Wu, F.X., 2021. Diagnosis of autism spectrum disorder based on functional brain networks with deep learning. *Journal of Computational Biology* 28, 146–165.
- Zeng, X., Gong, J., Li, W., Yang, Z., 2025. Knowledge-driven multi-graph convolutional network for brain network analysis and potential biomarker discovery. *Medical Image Analysis* 99, 103368.
- Zhang, C., Song, D., Huang, C., Swami, A., Chawla, N.V., 2019. Heterogeneous graph neural network, in: *Proceedings of the 25th ACM SIGKDD international conference on knowledge discovery & data mining*, pp. 793–803.
- Zhang, H., Song, R., Wang, L., Zhang, L., Wang, D., Wang, C., Zhang, W., 2023a. Classification of brain disorders in rs-fmri via local-to-global graph neural networks. *IEEE Transactions on Medical Imaging* 42, 444–455. doi:10.1109/TMI.2022.3219260.
- Zhang, J., Xu, D., Lou, Y., Huang, Y., 2024. A novel multi-atlas fusion model based on contrastive learning for functional connectivity graph diagnosis, in: *ICASSP 2024-2024 IEEE International Conference on Acoustics, Speech and Signal Processing (ICASSP)*, IEEE. pp. 2295–2299.
- Zhang, S., Chen, X., Shen, X., Ren, B., Yu, Z., Yang, H., Jiang, X., Shen, D., Zhou, Y., Zhang, X.Y., 2023b. A-gcl: Adversarial graph contrastive learning for fmri analysis to diagnose neurodevelopmental disorders. *Medical Image Analysis* 90, 102932.
- Zhang, Y., Zhou, T., Wang, S., Liang, P., Zhang, Y., Chen, D.Z., 2023c. Input augmentation with sam: Boosting medical image segmentation with segmentation foundation model, in: *International Conference on Medical Image Computing and Computer-Assisted Intervention*, Springer. pp. 129–139.
- Zheng, S., Zhu, Z., Liu, Z., Guo, Z., Liu, Y., Yang, Y., Zhao, Y., 2022. Multimodal graph learning for disease prediction. *IEEE Transactions on Medical Imaging* 41, 2207–2216.
- Zhu, Q., Wang, H., Xu, B., Zhang, Z., Shao, W., Zhang, D., 2022. Multimodal triplet attention network for brain disease diagnosis. *IEEE Transactions on Medical Imaging* 41, 3884–3894.
- Zuo, Q., Wu, H., Chen, C.P., Lei, B., Wang, S., 2024. Prior-guided adversarial learning with hypergraph for predicting abnormal connections in alzheimer’s disease. *IEEE Transactions on Cybernetics* .